Dysregulation of cholesterol and bile acid homeostasis across the gut-liver axis following *Cryptosporidium* intestinal infection

Shuhong Wang[1], Ai-Yu Gong[1], Edward Barker[1], David L. Williams[1], Christopher Forsyth[2], Liqing Yu[3], and Xian-Ming Chen[1,4]

[1]Department of Microbial Pathogens and Immunity, Rush University Medical Center, Chicago, Illinois, USA; [2]Department of Anatomy and Cell Biology, Rush University Medical Center, Chicago, Illinois, USA; [3]Division of Endocrinology, Diabetes and Nutrition, Department of Medicine, University of Maryland School of Medicine, Baltimore, Maryland 21201, USA.

[4]Correspondence: xian_m_chen@rush.edu

Abstract
Cryptosporidium spp., an apicomplexan protozoan, is one of the most common pathogens responsible for moderate-to-severe diarrhea in children under 2-year-old and an important opportunistic pathogen for patients with AIDS. There are no effective vaccines and therapy available. Infection in children is associated with malnutrition, growth defect and even impaired cognitive development but underlying mechanisms remain unclear. We report here that *C. parvum* infection in neonatal mice impairs bile acid reabsorption in the ileum and disturbs lipid metabolism in the liver and bile acid homeostasis in the enterohepatic circulation. Reduction of bile acid pool further impairs lipid absorption in the small intestine. Moreover, replenishing bile prevents decrease of lipid absorption in the infected neonatal mice. Strikingly, bile gavage significantly reduces the infection burden and ameliorates the dysregulated homeostasis of cell proliferation and migration in intestinal epithelium following infection. These findings may guide novel therapeutic approaches for cryptosporidiosis.

Introduction
Cryptosporidium is an important opportunistic intestinal pathogen for immunocompromised individuals and one of the common pathogens responsible for moderate-to-severe diarrhea in children under 2-year-old[1]. Infection with this parasite in young kids is associated with mortality, growth stunting, and developmental deficits[2]. Recent estimates from the Global Burden of Diseases, Injuries, and Risk Factors Study (GBD) suggest *Cryptosporidium* spp. is responsible for approximately 7.6 million cases and between 48,000 and 202,000 deaths annually among young children in low-resource settings[3,4]. Cryptosporidiosis in humans is primarily caused by *C. parvum* and *C. hominis* species[2]. Nitazoxanide, the only approved drug for the treatment of cryptosporidiosis, is ineffective in immunocompromised patients and not available for malnourished children[2,5–7]. Pathologically, *Cryptosporidium* infections are mainly confined in the distal ileum and it is speculated that the combined loss of microvillus borders and villus height reduces the absorptive intestinal surface, leading to malnutrition with diarrhea in children[8]. Nevertheless, current understanding of the underlying molecular mechanisms of malnutrition is still obscure, hampering the development of effective therapeutics. The intestinal mucosa is a monolayer of rapidly self-renewing epithelial cells. Intestinal stem cells in the crypts generate new functional epithelial cells that mature and differentiate as they progress up the villus before being shed at the tip[9,10]. *Cryptosporidium* infection is limited to the villi (mainly enterocytes) of intestinal epithelium as the organism forms an intracellular but extra-cytoplasmic parasitophorous vacuole at the brush border after its cell entry[11]. Increased cell death during infection triggers crypt hyperplasia and branching due to acceleration of cell division to compensate for cell loss at the villi[8,12].

As a major source of nutrition for infants, milk provides a large amount of fatty acids, phospholipids and cholesterol. Bile acids (BAs) are amphipathic molecules synthesized from cholesterol in the liver, stored in the gallbladder and are released into the duodenum after a meal[13]. BAs facilitate the emulsification of insoluble lipids into tiny mixed micelles, promoting lipid digestion and absorption in the intestine[14]. More than 95% of the BAs are reabsorbed in the terminal ileum through the apical sodium-dependent bile salt transporter (ASBT; SLC10A2) and recirculated to the liver via the portal blood in a process called enterohepatic circulation[13]. Farnesoid X receptor (FXR) is a ligand-activated transcription factor within the nuclear receptor (NR)-family and BAs are identified as endogenous FXR ligands with high affinity[15–17]. Thus, the

BA-FXR network plays an essential role for the maintenance of whole-body BA homeostasis by regulating the expression of target genes involved in both hepatic BA synthesis and enterohepatic circulation[18]. Using a murine neonatal infection model, here we report that *Cryptosporidium* infection causes significant disturbance of BA and lipid homeostasis both in the intestine and in the liver. Functionally, bile intervention greatly reduces infection burden, increases intestinal lipid absorption and ameliorates the dysregulated intestinal homeostasis and thus, may be of therapeutic potential for intestinal cryptosporidiosis.

Results

C. parvum infection disrupts cholesterol homeostasis in the small intestine

Consistent with results from previous studies[19], RNA-Seq analysis of ileum epithelium from infected neonatal mice [5-days old, 72h post-infection (p.i.)] reveals increased expression of many inflammatory and defense genes, including interferon-stimulated genes (ISGs), in the course of *C. parvum* infection (Supplementary Table 1). Gene set enrichment analysis (GSEA) of the RNA-Seq data indicates significant alterations in the expression levels of genes that control the sterol homeostasis in the infected ileum epithelium (Extended Data Fig. 2b). The cellular cholesterol homeostasis is finely controlled through the dynamic balance between biosynthesis, uptake, export and esterification[20]. Regulation of cellular cholesterol transport involves the low-density lipoprotein receptor (LDLR)-mediated absorption and chylomicron secretion, as well as transmembrane influx/efflux through transporters including Niemann-Pick C1-Like 1 (NPC1L1), the heterodimeric ATP-binding cassette transporters G5 and G8 (ABCG5/G8), and ATP-binding cassette transporter A1 (ABCA1) (Fig. 1a), which is governed by intricate feedback regulation mechanisms including the liver X receptor (LXR) signaling[21]. Further GSEA analysis indicates that cholesterol efflux, import and esterase activity were significantly downregulated (Fig. 1b and Extended Data Fig. 2a,b), while most genes involved in cholesterol biosynthesis were increased (Fig. 1b). Specifically, decreased expression levels of several cholesterol efflux genes, including ABCG5, ABCG8 and ABCA1, were confirmed by reverse transcription–quantitative PCR (RT–qPCR) (Fig. 1e). Consistent with this, immunoblot analyses of membrane protein and cytosolic protein extracts from the ileal epithelium from infected and control mice (72 h and 96 h p.i.) and immunofluorescence staining of ABCA1 (72 h p.i.) confirmed the reduced protein levels of ABCG5, ABCG8 and ABCA1 (Fig. 1c,d). Two LXRs, LXRα (NR1H3) and LXRβ (NR1H2), are important to transcriptional regulation of genes for cholesterol homeostasis[21]. Interestingly, the protein level of LXRβ was decreased while LXRα protein level remained unchanged in the ileum of infected neonates compared with the control groups (72 h and 96 h p.i.) (Fig. 1d), suggesting repression of LXR pathway after infection. In contrast, most of the cholesterol biosynthesis genes were upregulated following *C. parvum* infection (Fig. 1b), which was validated by RT-qPCR (Fig. 1f). The rate-limiting enzyme for cholesterol biosynthesis is 3-hydroxy-3-methylglutaryl-CoA reductase (HMGCR) and immunoblot analyses of membrane protein and cytosolic protein confirmed the higher level of HMGCR protein in the ileum of infected neonates compared with the control groups (Fig. 1d). Using Filipin III staining, we found that the level of free cholesterol in the ileum of infected neonatal mice was lower than that of the control mice (Fig. 1g).

Strikingly, the proximal small intestine (proximal SI, mainly responsible for digestion and nutrient absorption), which is not infected with *C. parvum* (Extended Data Fig. 1a,b), also showed similar changes in the expression levels of cholesterol homeostasis genes (Extended Data Fig. 2c-f). Notably, RT-qPCR showed an increased expression of NPC1L1 in the proximal

small intestine but a decreased expression in the ileum (Fig. 1e and Extended Data Fig. 2c). Moreover, considerable reduction in total cholesterol was detected in the proximal SI epithelium of infected neonates compared with their control groups (Fig. 3h and Extended Data Fig. 6a). Most of the cholesterol taken up by the intestine is secreted as chylomicrons into the circulation[22]. Expression of genes related to the chylomicron assembly was significantly downregulated in the proximal SI and ileum after infection (Extended Data Fig. 2g-i). Additionally, the small intestine of infected neonates was considerably shorter than those of controls (Extended Data Fig. 2j,k), suggesting a reduced absorptive intestinal surface area. Collectively, these results suggest that *C. parvum* infection disrupts cholesterol homeostasis in the small intestine.

C. parvum infection alters hepatic lipid metabolism

The liver is the major organ for cholesterol metabolism and most lipids in the intestine are taken up by enterocytes in the small intestine, transported through the lymphatic system into the circulation to the liver, and eventually to peripheral tissues[23,24]. We then hypothesized that *C. parvum* infection in the intestine could impact cholesterol and bile acid metabolism in the liver. We infected the neonatal mice with *C. parvum* oocysts for 3 days, collected the liver tissues and performed RNA-seq (Fig. 2a). Consistent with our hypothesis, *C. parvum* infection caused significant alterations in gene expression profiles in the liver (Extended Data Fig. 3a). GSEA indicated that the major pathways associated with the altered gene expression profiles are related to immune response regulation (Extended Data Fig. 3a). Gene set variation analysis (GSVA) reveals an overall down-regulation of genes for pathways of lipid metabolism in the liver from infected mice, including cholesterol and BA metabolic processes (Fig. 2c and Extended Data Fig. 3g). RT-qPCR further validated the reduced levels of most genes involved in the lipid metabolism (Extended Data Fig. 3b-f). Immunoblot analyses of APOB100 (Apolipoprotein B100), HMGCR and HMGCS2 (hydroxymethylglutaryl CoA synthase 2) confirmed their reduced protein levels in the infected animals (Extended Data Fig. 3h). The protein levels of hepatic FXR and LXRβ were drastically decreased whereas LXRα remained unchanged after infection (Fig. 2g). Consistent with this, the mRNA expression of most FXR and LXR target genes was significantly reduced in the livers of infected mice (Fig. 2b,d). Immunoblot and immunofluorescence staining of canonical target genes of LXRs and FXRs, including *ABCA1*, *ABCG5*, *ABCG8*, *CYP7A1* and *NR0B2* (*Shp*), confirmed their decreased protein levels (Fig. 2e-g). Accordingly, lipidomics analysis reveals altered levels of lipid profiles in the liver of infected mice (Fig. 2a and Extended Data Fig. 4a). It displayed no significant reduction in total lipids compared with the control group in the liver after 4 days infection (Extended Data Fig. 4b,c). However, reduced amounts of BAs and cholesterol ester, but not total cholesterol, were detected in the liver from infected mice (Fig. 2h and Extended Data Fig. 4d-f). As an important component of milk, fat supplies about 50% of the energy for infants[25]. The main fat component is triacylglycerol (TG), which make up more than 98% of milk fat[26]. We observed great reductions of most TGs, diacylglycerols (DG) and free fatty acids (FFA) in the liver after *C. parvum* intestinal infection (Fig. 2h and Extended Data Fig. 4g-l). KEGG pathway enrichment analysis of lipidomics results reveals downregulation of lipid metabolic pathways in the liver from infected mice (Extended Data Fig. 4m), which was in line with the GSVA results of RNA-seq (Fig. 2c and Extended Data Fig. 3g). To further investigate the alterations of BAs, we performed a comprehensive, quantitative bile acid targeted assay (Fig. 2a), showing a broad metabolic downregulation in the liver of infected mice (Fig. 2i,j). Taken together, the above data

indicate that *C. parvum* intestinal infection disturbs cholesterol and bile acid homeostasis in the liver.

C. parvum infection decreases BA levels in the small intestine and reduces the absorption of dietary lipids

Given the significant dysregulation of cholesterol and bile acid homeostasis in the liver after *C. parvum* intestinal infection, in particular the decreased expression of FXR-targeted genes, we next investigated the lipid metabolism with a focus on the BA-FXR signaling pathway in the infected intestine. FXR is essential for the maintenance of whole-body BA homeostasis through regulating the expression of target genes involved in both hepatic BA synthesis and enterohepatic circulation[18]. The enterohepatic circulation of BAs and the FXR pathway involve with the synthesis of BAs from cholesterol in the liver and fine-controlled expression of genes for BA reabsorption by the FXR signaling in the intestinal epithelium as shown in Fig. 3a. GSEA indicates that many genes for the BA metabolic process in the ileum were significantly reduced in the infected mice (Fig. 3b). The reduction of FXR and FXR-targeted genes *Shp* and *Fgf15* indicates a robust suppression of the FXR signaling in the small intestine following infection (Fig. 3b,d,e and Extended Data Fig. 5a). BAs generate negative feedback on ileal ASBT transcription by FXR-mediated induction of *Shp*[27]. Of note, despite a substantially increased expression at its mRNA level (Fig. 3b,d), ASBT was significantly reduced at the protein level (Fig. 3f).

To address whether dysregulation of liver and intestinal BA metabolism may change the bile levels in the small intestine following infection, we infected the neonatal mice with *C. parvum* oocysts for 4 days, collected the small intestine tissues (including the luminal contents), and performed a comprehensive, quantitative bile acid targeted assay. Marked decrease of total intestinal BAs was seen in the infected mice (Fig. 3g). Indeed, we observed a whiter ileum and ileal cell pellets, suggesting decreased intestinal BAs after infection (Fig. 3c). RNA-seq analysis of ileal tissues reveals a globally decreased expression of genes for lipid absorption in the infected mice (Extended Data Fig. 5f). Oil red O (ORO) staining showed that neutral lipids in the duodenum, jejunum, and ileum were reduced following infection (Fig. 3j). Accordingly, lipidomics analysis shows a significant decrease of total lipids (Fig. 3i), particularly of cholesterol, phosphatidylcholines (PC), hexosylceramides (HexCer-NS) and Ceramide-NS (Cer-NS) in the proximal SI epithelium from infected neonates (Fig. 3h and Extended Data Fig. 6a). However, lipidomics analysis shows no significant alteration of total TG level (Fig. 3h and Extended Data Fig. 6a). Additionally, proximal SI epithelium and ileum from infected neonates displayed reduced expression of several genes important for fatty acid oxidation, TG catabolism (Extended Data Fig. 5b-e), and chylomicron assembly (Extended Data Fig. 2g-i). Furthermore, reduced amounts of L-palmitoylcarnitine were detected in the proximal small intestinal epithelium of *C. parvum* infected neonates (Extended Data Fig. 6b), indicative of impaired fatty acid oxidation. All of these may contribute to the accumulation of TG in the proximal small intestinal epithelium following infection. Linoleic acid is an essential lipid that cannot be synthesized in mammalian cells and is exclusively acquired from the diet[28]. KEGG pathway enrichment analysis of lipidomics reveals suppression of linoleic acid metabolism (Extended Data Fig. 6c), further confirming the reduced absorption of dietary lipids in the intestine following *C. parvum* infection.

BA-FXR signaling pathway regulates the dysregulated homeostasis in the intestinal epithelium following *C. parvum* infection

To monitor the cell proliferation and epithelial turnover in the intestine following infection, we examined the incorporation and migration of ethynyl-2'-deoxyuridine (EdU)-labeled cells at 4, 24, and 48 h after EdU pulse labeling (Fig. 4a). To explore the potential effects of bile, we also administrated via oral gavage at 24 h p.i. the whole bile collected from the gallbladders of adult mice (Fig. 4a). As shown in Fig. 4b and 4c, there was a significant increase in the number of EdU-positive proliferating cells in the crypt regions of infected mice at 4 h, and these proliferative cells migrated much higher along the villus than they did in their control counterparts at 24 and 48 h p.i. (Fig. 4d-f). Interestingly, bile treatment significantly decreased the epithelial cell proliferation and migration in the infected intestinal epithelium (Figure 4b-f). Of note, we found that the dysregulation of cell proliferation and migration induced by infection, as well as the effects of bile supplement, was not limited to the ileum where *C. parvum* infected, but to the entire small intestine and even the colon (Fig. 4b-f). To test whether bile activates the FXR pathway to inhibit associated epithelial cell proliferation and migration, we treated *C. parvum* infected mice with the FXR agonist FexD and measured its effect on crypt cell proliferation and migration (Extended Data Fig. 7a). EdU-labeling analysis demonstrates a considerable decrease in EdU-positive proliferating and migrating cells in the infected mice treated with FexD compared to those treated with vehicle (Extended Data Fig. 7b-e). These data suggest that the BA-FXR signaling pathway may play a role in the cell proliferation and migration of the intestinal epithelium following *C. parvum* infection.

Bile intervention promotes intestinal anti-*C. parvum* defense and prevents decreased lipid absorption following *C. parvum* infection

To assess the impact of reduced bile on the pathogenesis of *C. parvum* infection, we next administered whole bile collected from the gallbladders of adult mice to C57BL/6 5 days old neonates at 24 h after oral gavage of *C. parvum* oocysts, followed by daily administration of bile for another 3 days (Fig. 5a). Bile feeding activated intestinal transcription of FXR target genes (Fig. 5c) and markedly decreased the infection burden compared to the animals receiving PBS (Fig. 5b). Significant reductions in the infected area from distal ileum and infection burden were observed in the intestinal tissues from infected animals receiving bile compared to the PBS-treated control group (Fig. 5e,f). In addition, replenishing bile prevented decreased lipid absorption and restored the ileal expression of genes associated with cholesterol homeostasis in the infected mice (Fig. 5d and Extended Data Fig. 8a-c). Moreover, human intestinal epithelial HCT-8 cells were first exposed to *C. parvum* infection for 4 h (a time frame for parasite attachment and invasion)[29] and free-parasites were removed after washing. The cell cultures were then exposed to different concentrations of bile or PBS for additional 20 h followed by measurement of infection burden. A substantial reduction in infection burden was observed in cells treated with the higher concentrations of bile (0.5% and 1%) compared with lower bile concentrations (0.2%, 0.25% and 0.33%) (Fig. 5g and Extended Data Fig. 8d). Interestingly, an increased infection burden was observed in the cultures treated with the low concentrations of bile compared to the PBS group (Fig. 5g and Extended Data Fig. 8d). Data from previous reports demonstrate that bile salt sodium taurocholate increases excystation and the entry of *Cryptosporidium* into host cells[30]. Accordingly, we observed an overall increased infection burden when HCT-8 cells were exposed to *C. parvum* oocysts in the presence of different concentration of bile (from 0.07%-2% BAs as tested) during the 4 h parasite attachment and

invasion time frame (Extended Data Fig. 8e). HCT-8 cells exposed to various concentrations of bile in the presence or absence of *C. parvum* showed no significant reduction of cell viability (Extended Data Fig. 9a-d).

Discussion

Cryptosporidium is referred to as a "minimal invasion" pathogen and the unique apical localization (intracellular but extra-cytoplasmic) after cell entry prevents its infection from further spreading to the deep epithelial tissues or into the circulation to other organs[31]. In addition, the infection is generally localized at the ileal region of the small intestine[32]. The marked alterations in gene expression profiles and metabolic processes in the liver and in the duodenum and jejunum regions in the small intestine from the current study indicate the pathological changes beyond the directly infected ileal region of the small intestine. From a pathological view point, the metabolic dysregulation beyond the ileum may be an important pathological factor for the growth stunting and malnutrition observed in young children following cryptosporidial infection.

The correlation of lipid and BA metabolic dysregulation revealed in the liver and intestine from infected mice provides another example for the role of the gut-liver axis in the pathogenesis of various enteritis. Given the primary infection site of *Cryptosporidium* in the ileum where over 95% of the BAs are reabsorbed[13], it maybe pathologically important that the expression of ASBT is downregulated at the protein level in the infected ileum, which may be a major factor for the decreased BA levels in the enterohepatic circulation. Depletion of intestinal cholesterol may also contribute to the decreased BA pool as ASBT function is dependent on the cholesterol content of lipid raft domains of the plasma membrane[33]. Moreover, the decreased absorptive intestinal surface due to the loss of microvillus borders and villus height following *Cryptosporidium* infection could reduce the brush border apical surface. Surprisingly, the reduction of the BA pool and the downregulation of the FXR pathway in the enterohepatic circulation following *C. parvum* infection did not increase hepatic bile synthesis as a compensation, but rather an overall decrease in bile acid metabolism in the liver. Reduced intestinal cholesterol absorption may contribute to the impaired bile synthesis in the liver. In addition, hepatic bile synthesis only accounts for a small fraction of BA pool as over 95% BA are preserved via enterohepatic circulation[34]. A recent report from Hu et al. identifies a hormone, Cholesin, which is secreted from the intestine in response to cholesterol absorption, exerting the inhibitory effect on hepatic cholesterol synthesis[35]. Our data suggest reduced intestinal cholesterol absorption and hepatic cholesterol synthesis following *C. parvum* infection and underlying mechanisms merit further investigation. Most BAs are transported back into the liver via enterohepatic circulation, a small fraction of this pool (roughly 5%) escapes reabsorption in the ileum, and further converted to form secondary BAs in the colon by the gut microbiota[13]. Several secondary BAs have been reported to impair growth of *Cryptosporidium in vitro*[36]. The bile salt sodium taurocholate enhances microneme secretion and increases the entry of *Cryptosporidium* into host cells[30]. Our studies confirmed that bile collected from the gallbladder of adult mice can enhance the infection of *Cryptosporidium* into host epithelial cells. However, sufficient supplement of collected bile can significantly reduce the infection burden both *in vivo* and *in vitro*. In addition, treatment with bile collected from the gallbladder of adult mice or FXR agonist FexD ameliorates the dysregulated cell proliferation and migration in the intestine, including directly infected ileum region and the non-infected regions, such as duodenum, jejunum, and the colon, indicating that

amelioration of such pathological features is not solely due to cell death caused by *Cryptosporidium* direct infection. Several studies have suggested a significant association between cryptosporidiosis and the presence of digestive neoplasia[37]. *C. parvum* ileal infection and subsequent dysregulation of lipid and BA metabolism on the cell proliferation and migration probably all contribute to the digestive neoplasia following *Cryptosporidium* infection. Our findings from this study could be relevant for the understanding of the mechanisms that cause intestinal complications associated with the severe inability to gain weight, digestive neoplasia, and shed light on BA-mediated anti-*C. parvum* defense following infection.

BAs have been reported to drive the newborn's gut microbiota maturation[38]. Gut microbiome development correlates with the development of the child. Changes in the composition and maturity of the gut microbiome could impact immune functions, intestinal development, neurodevelopment, nutritional energy harvest, growth, and weight gain[39]. The composition and diversity of the gut microbiome during early development play a crucial role in the incidence and severity of *Cryptosporidium* infection[40–42]. Whether bile treatment affects the maturation of the gut microbiota and thus improves long-term deficits in growth, weight gain, and cognitive development following *Cryptosporidium* infection merits further exploration.

Methods

Ethics statement

All research studies involving the use of animals were reviewed and approved by Institutional Animal Care and Use Committee (IACUC) of the Rush University at Chicago, Illinois and were carried out in strict accordance with the recommendations in the Guide for the Care and Use of Laboratory Animals.

C. parvum and Cell lines

C. parvum oocysts of the Iowa strain were purchased from a commercial source (Bunch Grass Farm, Deary, ID). HCT-8 cells were purchased from ATCC (Manassas, Virginia). Culture media were supplied with 10% fetal bovine serum (FBS) (Ambion, Austin, Texas) and antibiotics (100 IU/ml of penicillin and 100 μg/ml of streptomycin).

In vitro C. parvum infection experiments

Models of intestinal cryptosporidiosis using cultured cell lines were employed as previously described[43]. For *C. parvum* infection burden experiments, infection was done in serum-free culture medium for 4 h with a 1:4 ratio of *C. parvum* oocysts and HCT-8 cells, and culture medium was changed to remove free parasite. The culture medium was supplemented with mouse bile at a concentration of 0.2%, 0.25%, 0.33%, 0.5% and 1% (collected by gall bladder puncture of healthy adult C57BL/6 mice), respectively, and cultured for additional 20 h (a total 24 h p.i.) followed by infection burden measurement. Infection burden was quantified by measuring levels of *C. parvum* 18S (*cp18S*) gene[44]. Immunofluorescent staining of *C. parvum* was carried out using the rabbit antiserum against *C. parvum* membrane proteins as previously described[45,46]. For *C. parvum* invasion experiments, HCT-8 cells were incubated with *C. parvum* oocysts (1:4 ratio of oocysts to cells) in the presence of different concentration of bile (0.07%, 0.2%, 1%, and 2%) or PBS for 4 h, followed by RT-qPCR of *cp18S*.

In vivo C. parvum infection experiments

A well-developed infection model of cryptosporidiosis in neonatal mice was used for *in vivo* experiments[47,48]. Neonatal mice (5 days old) were orally inoculated with *C. parvum* (10^6 oocysts per animal). Mice receiving PBS by oral gavage were used as control. At 72 and 96 h after *C. parvum* oocysts or PBS administration, animals were sacrificed, and intestine and liver tissues were collected for biochemical analyses. For *C. parvum* infection burden experiments, Neonatal mice (5 days old) were orally inoculated with *C. parvum* (10^5 oocysts per animal). At 24 h after *C. parvum* infection, animals were fed with PBS-diluted bile (7ul per animal,1:1 ratio of bile to PBS) and PBS (7ul per animal) respectively, followed by daily for 4 days. Animals were sacrificed, and intestine tissues were collected for biochemical analyses.

In vivo EdU assay

Neonatal mice (5 days old) were orally inoculated with *C. parvum* (10^5 oocysts per animal). Mice receiving PBS by oral gavage were used as control. For bile treatment, at 24 h after *C. parvum* oocysts or PBS administration, control mice were treated with PBS, *C. parvum* infected mice were fed with PBS-diluted bile (7ul per animal,1:1 ratio of bile to PBS) and PBS (7ul per animal) respectively, followed by daily for 3 days. Mice were i.p. injected with EdU and sacrificed at 4 h post injection; Mice were i.p. injected with EdU, treated with PBS-diluted bile or PBS for another 1 day and sacrificed at 24 h post injection; Mice were i.p. injected with EdU, treated with PBS-diluted bile or PBS for another 2 days and sacrificed at 48 h post injection. For FXR agonists fexaramine D (FexD) treatment, at 24 h after *C. parvum* oocysts or PBS administration, control mice were i.p. injected with vehicle, *C. parvum* infected mice were i.p. injected with vehicle with or without 100mg/kg of FexD, followed by daily for 3 days. Mice were i.p. injected with EdU and sacrificed at 4 h post injection; Mice were i.p. injected with EdU, treated with vehicle with or without FexD for another 2 days and sacrificed at 48 h post injection. Intestine tissues were frozen in OCT and cryosectioned (10 mm). EdU staining was conducted using Click-iT EdU imaging kit (Thermofisher cat# C10337) according to the manufacturer's protocol.

RT-qPCR

Total RNA was isolated using TRIzol™ Reagent (Thermo Fisher Scientific, catalogue no. 15596018) and genomic DNA was removed with the DNA-free™ DNA Removal Kit (Thermo Fisher Scientific, catalogue no. AM1906). The reverse-transcription reaction was performed on 2 μg total RNA with M-MLV Reverse Transcriptase (Thermo Fisher Scientific, catalogue no. 28025013). Quantitative PCR assays were conducted on Bio-Rad CFX Manager v3.1 using the iTaq™ Universal SYBR® Green Supermix (Bio-rad, Hercules, CA, USA, catalogue no. 1725124). RNA expression levels were calculated using the ΔΔCt method.

RNA-Seq and bioinformatic analysis

Total RNAs isolated with Rneasy Mini Kit (QIAGEN, catalogue no. 74104). Three biological replicates (all mice from the same litter) were performed for each studied condition. The samples were analyzed by the BGI Americas Corporation (Cambridge, MA) with DNBSEQ™ sequencing technology platforms. Differential expression analysis and statistical significance calculations between conditions were assessed using DESeq in R using a standard negative binomial fit for the aligned counts data and are described relative to the indicated control (Supplementary Table 1 and 2). Gene set enrichment analysis (GSEA) was performed by R package "clusterProfiler"[49], using the gene sets from the MsigDB database (http://www.gsea-

msigdb.org/gsea/index.jsp)[50]. We performed gene set variation analysis (GSVA) with $p < 0.05$ to explore correlated pathways using the gene sets from the MsigDB database[51].

Immunoblotting

Membrane and cytosolic proteins were isolated from frozen mouse liver or small intestine (30mg) using the Mem-PER Plus Membrane Protein Extraction Kit (Thermo Fisher Scientific, Catalog no. 89842). Membrane and cytosolic fractions were separated by SDS-PAGE and transferred to a nitrocellulose membrane. Images were generated using the ChemiDoc MP Imaging System (Bio-Rad, Catalog no. 12003154). The following primary and secondary antibodies were used: anti-β Tubulin (Santa Cruz, catalogue no. sc-5274, 1:1000), anti-GAPDH (Santa Cruz, catalogue no. sc-32233, 1:1000), anti-ABCG5 (Thermo Fisher Scientific, catalogue no. BS-5013R, 1:1000), anti-ABCG8 (Novus Biologicals, catalogue no. 1B10A5, 1:1000), anti-SLC10A2 (Abcam, catalogue no. ab203205, 1:1000), anti-FGF15 (Santa Cruz, catalogue no. sc-514647, 1:1000), anti-NR1H4 (Proteintech, catalogue no. 25055-1-AP, 1:3000), anti-NR1H3 (Proteintech, catalogue no. 14351-1-AP, 1:5000), anti-NR1H2 (Proteintech, catalogue no. 60345-1-Ig, 1:1000), anti-Na+/K+-ATPase (Abclonal, catalogue no. A12405, 1:2000), anti-HMGCR (Abclonal, catalogue no. A1633, 1:2000), anti-CYP7A1 (Abclonal, catalogue no. A10615, 1:1000), anti-NR0B2 (Abclonal, catalogue no. A1836, 1:500), anti-HMGCS2 (Abclonal, catalogue no. A19232, 1:2000), anti-rabbit B700 (Bio-Rad, catalogue no. 12004161, 1:2500), anti-mouse B700 (Bio-Rad, catalogue no. 12004158, 1:2500), anti-rabbit B520 (Bio-Rad, catalogue no. 12005869, 1:2500), anti-mouse B520 (Bio-Rad, catalogue no. 12005866, 1:2500), anti-GAPDH hFAB™ Rhodamine (Bio-Rad, catalogue no. 12004167, 1:2500), anti-Tubulin hFAB™ Rhodamine (Bio-Rad, catalogue no. 12004165, 1:2500).

Immunohistochemistry

For tissue staining, frozen sections (8 μm) were fixed in 4% PFA in PBS for 15 min, and then washed twice with PBS. Add 0.5% Triton X-100 (Bio-rad, catalogue no. 1610407) in PBS for 20 min, remove permeabilization buffer and wash twice with PBS. Sections were blocked for 30 min in 10% normal donkey serum (NDS), 0.1% Triton X-100, 0.01% sodium azide in PBS, prior to incubation with primary antibody for 2 h at room temperature or overnight at 4 °C. Slides were then washed three times with PBS and incubated in block solution containing secondary antibody for 30 min at room temperature. Following antibody incubation, 3 × 5 min PBS washes were performed, and sections were mounted with Antifade Mounting Medium with DAPI (Vector, catalogue no. H-1200). Images were taken on a Keyence BZ-X810 microscope. For cell staining, HCT-8 cells were fixed in 4% PFA in PBS for 15 min and washed twice with PBS. Fixed cells were permeabilized in 0.1% Triton X-100 in PBS for 5 min and washed three times with PBS. Cells were blocked for 30 min in 10% NDS, 0.1% Triton X-100, 0.01% sodium azide in PBS, prior to incubation with primary antibody for 1 h at room temperature. Cells were then washed three times with PBS and incubated in block solution containing secondary antibody for 30 min at room temperature. Following antibody incubation, 3 × 5 min PBS washes were performed, and sections were mounted with Antifade Mounting Medium with DAPI (Vector, catalogue no. H-1200). Images were taken on a Keyence BZ-X810 microscope. Immunofluorescent staining of *C. parvum* was carried out using the rabbit antiserum against *C. parvum* membrane proteins as previously described[45,46]. Other antibodies used for immunofluorescent staining include anti-Ki67 antibody (Cell Signaling Technology, catalogue no. 9129, 1:200), anti-ABCA1 antibody (Thermo Fisher Scientific, catalogue no. PA1-16789, 1:200), goat-anti-bovine Alexa fluor 488 (Jackson Immuno Research, catalogue no. 101-545-003, 1:250), goat-anti-bovine Alexa fluor 594 (Jackson Immuno Research, catalogue no. 101-585- 003, 1:250), donkey-anti-rabbit Alexa fluor 488 (Jackson Immuno Research, catalogue no.

711-545-152, 1:500), donkey-anti-rabbit Rhodamine Red (Jackson Immuno Research, catalogue no. 711-295-152, 1:500).

Filipin staining

To quantify intracellular cholesterol levels, frozen sections (5 μm) of tissues were cut and stained with Filipin (Sigma, catalogue no. SAE0088; 5 mg in 1 ml DMSO). Briefly, sections were fixed in 4% PFA in PBS for 15 min, washed in 1× PBS, and then stained for 45 min in working Filipin solution (0.2 ml stock solution in 10 ml PBS). Samples were subsequently washed in 1× PBS, incubated in the nuclei marker DRAQ7 (Abcam, catalogue no. ab109202, 1:400 in 1× PBS) for 5 min, and then cover slipped using aqueous mounting medium (Abcam, catalogue no. ab128982). Images were taken on a Keyence BZ-X810 microscope.

Oil red staining

Lipid vesicle storage in tissue was assessed with Oil Red O staining in accordance with the manufacturer's protocol (Abcam, catalogue no. ab150678). Images were taken on a Keyence BZ-X810 microscope.

Cell viability

Cell viability was tested using a Neutral Red Assay Kit according to the manufacturer's instructions (Abcam, catalogue no. ab234039). The absorbance of each well at 540 nm was measured by a microplate reader (SpectraMax iD3, Molecular Devices, USA) to examine the cell viability.

Bile Acid Targeted Metabolomics Assay

Metabolites were extracted from the livers and small intestine of control and *C. parvum* infected neonatal mice, each condition in three biological replicates. The samples were analyzed by Wuhan Metware Biotechnology. Homogenize the sample by adding one steel bead to 20 mg of solid sample, 10 μl of 1 μg/ml internal standard working solution, and 200 μl of 20% methanol in acetonitrile; Shake the homogenized sample at 2500 rpm for 10 min, and then place it in a -20°C for 10 min; Centrifuge at 4°C, 12,000 rpm for 10 min. Then collect the supernatant and concentrate it in a concentrator; After the concentration is completed, reconstitute the sample with 100 μl of 50% methanol-water solution, and set it aside for subsequent LC-MS/MS. The sample extracts were analyzed using an LC-ESI-MS/MS system (UPLC, ExionLC™ AD, https://sciex.com/; MS, QTRAP® 6500+, https://sciex.com/). The analytical conditions were as follows, HPLC: column, Waters ACQUITY UPLC HSS T3 C18 (100 mm×2.1 mm i.d., 1.8 μm); Solvent system, water with 0.01% acetic acid and 5 mmol/L ammonium acetate (A), acetonitrile with 0.01% acetic acid (B); The gradient was optimized at A/B 95:5 (V/V) at 0 min, A/B 60:40 (V/V) at 0.5 min, 50:50 (V/V) at 4.5 min, 25:75 (V/V) at 7.5 min, 5:95 (V/V) at 10 min, 95:5 (V/V) at 12.0 min ; Flow rate, 0.35 mL/min; Temperature, 40°C; Injection volume: 3 μl. The effluent was alternatively connected to an ESI-triple quadrupole-linear ion trap (QTRAP)-MS. LIT and triple quadrupole (QQQ) scans were acquired on a triple quadrupole-linear ion trap mass spectrometer (QTRAP), QTRAP® 6500+ LC-MS/MS System, equipped with an ESI Turbo Ion-Spray interface, operating in negative ion mode and controlled by Analyst 1.6.3 software (Sciex). The ESI source operation parameters were as follows: Ion source, ESI-; Source temperature 550 ℃; Ion spray voltage (IS)-4500 V; Curtain gas (CUR) was set at 35 psi, respectively. Bile acids were analyzed using scheduled multiple reaction monitoring (MRM). Data acquisitions were performed using Analyst 1.6.3 software (Sciex). Multiquant 3.0.3 software (Sciex) was

used to quantify all metabolites. Mass spectrometer parameters including the declustering potentials (DP) and collision energies (CE) for individual MRM transitions were done with further DP and CE optimization. A specific set of MRM transitions were monitored for each period according to the metabolites eluted within this period.

Quantitative Lipidomics

Metabolites were extracted from the livers and proximal IECs of control and *C. parvum* infected neonatal mice, each condition in four biological replicates. The samples were analyzed by Wuhan Metware Biotechnology. Metabolomics profiling was employed as previously described[52].

Bioinformatic analysis of metabolomics

Multivariate analysis of Variable Importance in Projection (VIP) from OPLS-DA modeling (MetaboAnalystR, v.1.0.1) was used to preliminarily select differential metabolites from different samples. For two-group analysis, differential metabolites were determined by VIP (VIP > 1) and P-value (P-value < 0.05, Student's t test). The data was log transform (log_2) and mean centering before OPLS-DA. To avoid overfitting, a permutation test (200 permutations) was performed. For KEGG annotation and enrichment analysis, identified lipids were annotated using KEGG Compound database (http://www.kegg.jp/kegg/compound/), annotated lipids were then mapped to KEGG Pathway database (http://www.kegg.jp/kegg/pathway.html). Pathways with significantly regulated lipids mapped to were then fed into MSEA (lipid sets enrichment analysis), their significance was determined by hypergeometric test's p-values.

Statistical analysis

For all quantitative analyses, a minimum of three biological replicates were analyzed. Statistical tests were selected on the basis of the assumption that sample data are from a population following a probability distribution based on a fixed set of parameters. Student's t-tests were used to determine the statistical significance of differences between two groups. One-way AVOVA was used for multiple comparison tests. The following values were considered to be statistically significant: *P < 0.05, **P < 0.01, ***P < 0.001, ****P < 0.0001. Calculations were carried out using the GraphPad Prism 10 software package. Data are represented as mean ± the standard error of the mean.

Data availability

The RNA-seq data generated in this study have been deposited into NCBI's Gene Expression Omnibus (GEO) and are accessible through GEO series accession number GSE234579 and GSE272799. The metabolomics analysis data are presented in Supplementary Table 3- 6. Uncropped images of immunoblots presented in the figures are included in Supplementary Fig. 1. Source data are provided with this paper.

Figure legends

Fig. 1 | *C. parvum* infection disrupts cholesterol homeostasis in ileum. a, Schematic diagram summarizing the molecular mechanism of cholesterol transport. **b,** Cholesterol homeostasis gene expression changes upon *C. parvum* infection (72 h) in 5 days old neonatal mouses. The enrichment of cholesterol biosynthesis and efflux gene sets is shown at the bottom. The upregulated and downregulated genes (log2FC > 0.5, adj. p < 0.05) are indicated by the light

red– and light blue–shaded rectangles underlaid on plot, respectively. **c,** Immunofluorescence staining of ileal Abca1 in neonates with and without *C. parvum* infection (72 h p.i.). Blue: DAPI (nuclei), green: Abca1. Bars, 100 μm. **d,** Immunoblotting analysis of ileum samples in neonates with and without *C. parvum* infection (72 h and 96 h p.i.). Gapdh was used as loading control of cytosolic protein, Na+/K+ ATPase was used as loading control of membrane protein. **e, f,** Relative amounts of mRNAs analyzed by RT–qPCR (n = 4 biologically independent samples per group). Gene expression was presented as fold change to uninfected control. **g,** Filipin staining of endogenous cholesterol of ileum in neonates with and without *C. parvum* infection (72 h p.i.). Filipin III (blue) stains cholesterol, DRAQ7 (red) detects nuclei. Bars, 100 μm. Data are expressed as mean ± SEM. Statistical analysis: unpaired t test for (e, f); *P < 0.05, **P < 0.01, ***P < 0.001, ****P < 0.0001. For gel source data, see Supplementary Fig. 1. All mice from the same litter.

Fig. 2 | *C. parvum* intestinal infection causes dysregulation of cholesterol and bile acid homeostasis in the liver. a, Experiment schematics: Neonatal mice (5 days old) were orally inoculated with *C. parvum* oocysts (10^6 oocysts per animal) and liver tissues were collected for deep sequencing (72 h p.i.) and metabolomics (96 h p.i.). **b,** Heatmap of LXR and FXR target genes expression in the liver of *C. parvum* infected neonatal mice versus control mice (72 h p.i.). **c,** GSVA heatmap of bile and sterol metabolic pathways. **d,** RT-qPCR analysis confirming hepatic mRNA expression of LXR and FXR targeted genes in neonates with and without *C. parvum* infection at 72 h p.i (n = 5 biologically independent samples per group). **e,** Immunofluorescence staining of hepatic Abca1 in neonates with and without *C. parvum* infection (72 h p.i.). Blue: DAPI (nuclei), red: Abca1. Bars, 50 μm. **f, g,** Immunoblotting analysis of liver samples in control and *C. parvum* infected neonatal mice (72 h p.i.). Gapdh and α-tubulin were used as loading control of cytosolic protein, Na+/K+ ATPase was used as loading control of membrane protein. **h,** Scatter plot showing the change of hepatic lipids between control or *C. parvum* infected mice in different subclasses. Lipid with VIP ≥ 1 represents significant difference. **i,** Heatmap of differential hepatic BAs expression in control versus *C. parvum* infected mice. **j,** The total quantification of all BAs in liver between control and *C. parvum* infected neonatal mice from (i). Data are expressed as mean ± SEM. Statistical analysis: unpaired t test for (d, j); *P < 0.05, **P < 0.01, ***P < 0.001, ****P < 0.0001. For gel source data, see Supplementary Fig. 1. All mice from the same litter.

Fig. 3 | *C. parvum* infection decreases BA levels in the small intestine and reduces the absorption of dietary lipids. a, Schematic overview of the enterohepatic circulation of BAs and the FXR pathway. **b,** Differential gene expression analysis upon *C. parvum* infection (72 h) in 5 days old neonatal mouses. The enrichment of bile acid metabolic gene set is shown at the bottom. **c,** Representative images of ileum and ileal cell pellets. **d,** RT-qPCR analysis confirming ileum mRNA expression of Nr1h4, Fgf15, Nr0b2 and Slc10a2 from infected neonates (72 h p.i.). **e, f,** Immunoblotting analysis of ileum samples in control and *C. parvum* infected neonatal mice (72 h and 96 h p.i.). Gapdh was used as loading control of cytosolic protein, Na+/K+ ATPase was used as loading control of membrane protein. **g,** Heatmap of differential intestinal BAs expression in control versus *C. parvum* infected mice. Neonatal mice (5 days old) were orally inoculated with *C. parvum* oocysts (10^6 oocysts per animal) and small intestine was collected (96 h p.i.) for bile acid targeted assay. **h,** Scatter plot showing the change of proximal SI lipids between control or *C. parvum* infected mice in different subclasses. Neonatal mice (5 days old)

were orally inoculated with *C. parvum* oocysts (10^6 oocysts per animal) and proximal IECs were collected (96 h p.i.) for lipidomics analysis. Lipid with VIP ≥ 1 represents significant difference. **i,** The total quantification of all lipids in proximal SI between control and *C. parvum* infected neonatal mice. **j,** Oil Red O stains of the duodenum, jejunum and ileum section in neonates with and without *C. parvum* infection (96 h p.i.). Data are expressed as mean ± SEM. Statistical analysis: unpaired t test for (d, i); *P < 0.05, **P < 0.01, ***P < 0.001, ****P < 0.0001. For gel source data, see Supplementary Fig. 1. All mice from the same litter.

Fig. 4 | Bile intervention attenuates the dysregulated homeostasis in the intestinal epithelium following *C. parvum* infection. a, Experiment schematics: Neonatal mice (5 days old) were orally administered 1×10^5 *C. parvum* oocysts; PBS or bile were given at 24 h p.i. followed by daily for 3 days; Mice were i.p. injected with EdU and sacrificed at 4 h post injection; Mice were i.p. injected with EdU, treated with PBS or bile for another 1 day and sacrificed at 24 h post injection; Mice were i.p. injected with EdU, treated with PBS or bile for another 2 days and sacrificed at 48 h post injection. **b,** Representative images of Ki67, EdU staining of proliferating cells in crypts at 4 h post injection. Blue: DAPI (nuclei), red: Ki67, green: EdU. Bars, 50 μm. **c,** Quantification of EdU staining of proliferating cells in crypts at 4 h post injection. **d, e,** Representative images of Ki67, EdU staining of proliferating cells at 24 h (d) and 48 h (e) post injection. Blue: DAPI (nuclei), red: Ki67, green: EdU. Bars, 100 μm. **f,** Quantification of cell migration length along the crypt-villus axis at 48 h post injection. Quantification of cell migration length by measuring the distance from the crypt base to the highest labelled cell in the villus. One-way analysis of variance (ANOVA) with Tukey tests was used for correction of multiple comparisons in c and f; *P < 0.05, **P < 0.01, ***P < 0.001, ****P < 0.0001. All mice from the same litter.

Fig. 5 | Bile intervention promotes intestinal anti-*C. parvum* defense and prevents decreased lipid absorption following infection. a, Experiment schematics: Neonatal mice (5 days old) were orally administered 1×10^5 *C. parvum* oocysts; PBS and bile were given at 24 h p.i. followed by daily for 4 days, respectively; Intestinal tissues were collected, and the mRNA levels of infection burden (b) and FXR target genes (c) were measured by RT-qPCR. **d,** Oil Red O stains of the duodenum, jejunum and ileum sections from (a). **e, f,** Immunofluorescent staining of *C. parvum* from (a). A higher magnification of the boxed region to visualize the maximum infected area of *C. parvum* from distal ileum is shown (e). A higher magnification of the boxed region to visualize the infection burden of *C. parvum* from different portion of ileum is shown (f). Blue: DAPI, red: Ki67, green: *C. parvum*. Bars, 100 μm. **g,** Effects of bile on *C. parvum* infection of cultured HCT-8 cells. Cells were incubated with oocysts for 4 h first, subsequently exposed to different concentration of bile or PBS for another 20 h, followed by RT-qPCR of *cp18S* (*p<0.05 vs. PBS, ^ p<0.05 vs. 0.2% bile, #p<0.05 vs. 0.25% bile, + p<0.05 vs. 0.33% bile). Data are expressed as mean ± SEM. Statistical analysis: unpaired t test for (b, c), one-way analysis of variance (ANOVA) with Tukey tests was used for correction of multiple comparisons in g; *P < 0.05, **P < 0.01, ***P < 0.001, ****P < 0.0001. All mice from the same litter.

Extended Data Fig. 1 | *C. parvum* intestinal infection burden in neonates with and without *C. parvum* infection. a, Representative images of duodenum, jejunum and ileum sections from *C. parvum* infected and control mice immunostained for *C. parvum* and Ki67 (96 h p.i.). Blue: DAPI (nuclei), red: Ki67, green: *C. parvum*. Bars, 100 μm. **b,** Relative amounts of mRNAs

analysed by RT–qPCR (n = 4 biologically independent samples per group). Neonatal mice (5 days old) were inoculated with *C. parvum* oocysts (10^6 oocysts per animal) for 96 h. Infection burden was evaluated by RT-qPCR of *cp18S* gene in the duodenum, jejunum and ileum, respectively. The cycle threshold (Ct) values were used to determine the infection burden. Data are expressed as mean ± SEM. Statistical analysis: unpaired t test for (b); *P < 0.05, **P < 0.01, ***P < 0.001, ****P < 0.0001. All mice from the same litter.

Extended Data Fig. 2 | *C. parvum* infection disrupts cholesterol homeostasis in the small intestine. a, Differential gene expression analysis upon *C. parvum* infection (72 h) in 5 days old neonatal mouses. The enrichment of sterol esterase activity gene set is shown at the bottom. **b,** GSEA showing the enriched pathways of sterol homeostasis and sterol transport (|NES| > 1, p < 0.05, FDR < 0.25). **c, h, i,** Relative amounts of mRNAs analyzed by RT–qPCR (n = 4 biologically independent samples per group). Gene expression was presented as fold change to uninfected control. **d,** Immunofluorescence staining of Abca1 in neonates with and without C. parvum infection (72 h p.i.). Blue: DAPI (nuclei), green: Abca1. Bars, 100 µm. **e-g,** Immunoblotting analysis of proximal and ileal IECs samples. Gapdh and α- tubulin were used as loading control of cytosolic protein, Na+/K+ ATPase was used as loading control of membrane protein. **j,** Small intestine length of control and *C. parvum* infected mice (n=5 biologically independent samples per group). **k,** Representative images of small intestines from control and *C. parvum* infected mice (120 h p.i.). Data are expressed as mean ± SEM. Statistical analysis: unpaired t test for (c, h, i and j); *P < 0.05, **P < 0.01, ***P < 0.001, ****P < 0.0001. For gel source data, see Supplementary Fig. 1. All mice from the same litter.

Extended Data Fig. 3 | *C. parvum* infection alters hepatic genes expression. a, Differential hepatic gene expression analysis upon *C. parvum* infection (72 h) in 5 days old neonatal mouses. The enrichment of positive regulation of immune response gene set is shown at the bottom. **b-f,** Relative mRNA expression of lipid metabolic genes associated with the indicated processes were measured by RT-qPCR (n = 5 biologically independent samples per group). **g,** GSVA heatmap of lipid metabolic pathways. **h,** Immunoblotting analysis of liver samples in neonates with and without *C. parvum* infection (72 h p.i.). Gapdh and α-tubulin were used as loading control of cytosolic protein, Na+/K+ ATPase was used as loading control of membrane protein. Data are expressed as mean ± SEM. Statistical analysis: unpaired t test for (b-f); *P < 0.05, **P < 0.01, ***P < 0.001, ****P < 0.0001. For gel source data, see Supplementary Fig. 1. All mice from the same litter.

Extended Data Fig. 4 | Impaired lipid homeostasis in the livers of *C. parvum* infected mice. a, Volcano plot illustrating the hepatic lipids expression between control and *C. parvum* infected neonatal mice (96 h p.i.). Lipid with VIP ≥ 1 represents significant difference. **b,** Oil Red O stains of the liver sections in neonates with and without *C. parvum* infection (96 h p.i.). **c,** The total quantification of all hepatic lipids between control and *C. parvum* infected neonatal mice (96 h p.i.). **d-i,** Graphs depicting quantification of the differences in hepatic BA(d), CE(e), Cholesterol(f), FFA(g), DG(h) and TG(i) between control or *C. parvum* infected mice (96 h p.i.). **j, k, l,** Graphs showing the fold change of hepatic FFA(j), DG(k) and TG(l) with different chain lengths between control or *C. parvum* infected mice (96 h p.i.). Each point represents a lipid, the size of the point represents the P-value. **m,** KEGG pathway enrichment analysis and differential abundance (DA) scores of differential metabolites in the liver of control and *C. parvum* infected

neonatal mice (96 h p.i.). DA score = (up regulated lipids in a pathway-down regulated lipids in a pathway)/ (Total number of lipids annotation in a pathway). Data are expressed as mean ± SEM. Statistical analysis: unpaired t test for (c-i); *P < 0.05, **P < 0.01, ***P < 0.001, ****P < 0.0001. All mice from the same litter.

Extended Data Fig. 5 | *C. parvum* infection alters intestinal lipid metabolic genes expression. a-c, Relative amounts of mRNAs analyzed by RT–qPCR (n = 4 biologically independent samples per group). Gene expression was presented as fold change to uninfected control. **d,** Immunoblot analysis of proximal and ileal IECs from control and *C. parvum* infected neonatal mice (72 h and 96 h p.i.). Gapdh was used as loading control of cytosolic protein. **e, f,** GSEA showing the enriched pathways of fatty acid metabolic process (e) and intestinal lipid absorption process (f) (|NES| > 1, p < 0.05, FDR < 0.25). Data are expressed as mean ± SEM. Statistical analysis: unpaired t test for (a-c); *P < 0.05, **P < 0.01, ***P < 0.001, ****P < 0.0001. For gel source data, see Supplementary Fig. 1. All mice from the same litter.

Extended Data Fig. 6 | Impaired lipid homeostasis in the proximal IECs of *C. parvum* infected mice. a, Graphs depicting quantification of the differences in proximal SI lipid abundance of each subclass between control or *C. parvum* infected mice (96 h p.i.). **b,** Graphs showing the quantification of L-palmitoylcarnitine in proximal SI between control or *C. parvum* infected mice (96 h p.i.). **c,** KEGG pathway enrichment analysis and DA scores of differential metabolites in proximal SI of control and *C. parvum* infected neonatal mice (96 h p.i.). Data are expressed as mean ± SEM. Statistical analysis: unpaired t test for (a, b); *P < 0.05, **P < 0.01, ***P < 0.001, ****P < 0.0001. All mice from the same litter.

Extended Data Fig. 7 | FXR activation attenuates the dysregulated homeostasis in the intestinal epithelium following *C. parvum* infection. a, Experiment schematics: Five-day-old C57BL/6 neonates were orally administered 1×10^5 *C. parvum* oocysts; FexD or vehicle were given at 24 h p.i., followed by daily for 3 days; Mice were i.p. injected with EdU and sacrificed at 4 h post injection; Mice were i.p. injected with EdU, treated with FexD or vehicle for another 2 days and sacrificed at 48 h post injection. **b,** Representative images of Ki67, EdU staining of proliferating cells in crypts at 4 h post injection. Blue: DAPI (nuclei), red: Ki67, green: EdU. Bars, 50 µm. **c,** Quantification of EdU staining of proliferating cells in crypts at 4 h (b) post injection. **d,** Representative images of Ki67, EdU staining of proliferating cells at 48 h post injection. Blue: DAPI (nuclei), red: Ki67, green: EdU. Bars, 100 µm. **e,** Quantification of cell migration length along the crypt-villus axis at 48 h (d) post injection. Quantification of cell migration length by measuring the distance from the crypt base to the highest labelled cell in the villus. One-way analysis of variance (ANOVA) with Tukey tests was used for correction of multiple comparisons in c and e; *P < 0.05, **P < 0.01, ***P < 0.001, ****P < 0.0001. All mice from the same litter.

Extended Data Fig. 8 | Effects of bile on *C. parvum* infection. a, Effects of bile on *C. parvum* intestinal infection in neonates. Five-day-old C57BL/6 neonates were orally administered *C. parvum* oocysts; PBS and bile were given at 24 h p.i. followed by daily for 4 days, respectively; Intestinal tissues were collected, and the mRNA levels of cholesterol biosynthesis genes (a) and cholesterol efflux genes (b) were measured by RT-qPCR. Gene expression was presented as fold change to uninfected control. **c,** Filipin staining of endogenous cholesterol of duodenum,

jejunum and ileum in neonates from (a). Filipin III (blue) stains cholesterol, DRAQ7 (red) detects nuclei. Bars, 100 µm. **d,** Effects of bile on *C. parvum* infection of cultured HCT-8 cells. Cells were incubated with oocysts for 4 h first, subsequently exposed to different concentration of bile or PBS for another 20 h, followed by immunofluorescence staining of *C. parvum*. Blue: DAPI (nuclei), red: *C. parvum*. Bars, 100 µm. **e,** Effects of bile on *C. parvum* invasion of cultured HCT-8 cells. Cells were incubated with oocysts for 4 h in the presence of different concentration of bile or PBS, followed by RT-qPCR of *cp18S*. Data are expressed as mean ± SEM. Statistical analysis: unpaired t test for (a, b and e); *P < 0.05, **P < 0.01, ***P < 0.001, ****P < 0.0001. All mice from the same litter.

Extended Data Fig. 9 | Effects of bile on HCT-8 cells viability with or without *C. parvum* infection. a, Effects of bile on HCT-8 cells viability in the presence of *C. parvum* infection. Cells were incubated with oocysts for 4 h first, subsequently exposed to different concentration of bile or PBS for another 20 h, followed by cell viability assay. **b,** Cell survival of HCT-8 cells treated with different concentration of bile or PBS for 24 h. **c, d,** Cell survival of HCT-8 cells exposed to different concentration of bile or PBS with (c) or without (d) oocysts for 4 h. One-way analysis of variance (ANOVA) with Dunnett's multiple comparison test was used for correction of multiple comparisons in a-d; *P < 0.05, **P < 0.01, ***P < 0.001, ****P < 0.0001.

References

1. Kotloff, K. L. *et al.* Burden and aetiology of diarrhoeal disease in infants and young children in developing countries (the Global Enteric Multicenter Study, GEMS): a prospective, case-control study. *Lancet Lond. Engl.* **382**, 209–222 (2013).
2. Checkley, W. *et al.* A review of the global burden, novel diagnostics, therapeutics, and vaccine targets for cryptosporidium. *Lancet Infect. Dis.* **15**, 85–94 (2015).
3. Sow, S. O. *et al.* The Burden of Cryptosporidium Diarrheal Disease among Children < 24 Months of Age in Moderate/High Mortality Regions of Sub-Saharan Africa and South Asia, Utilizing Data from the Global Enteric Multicenter Study (GEMS). *PLoS Negl. Trop. Dis.* **10**, e0004729 (2016).
4. Khalil, I. A. *et al.* Morbidity, mortality, and long-term consequences associated with diarrhoea from Cryptosporidium infection in children younger than 5 years: a meta-analyses study. *Lancet Glob. Health* **6**, e758–e768 (2018).
5. Costa, L. B. *et al.* Cryptosporidium-malnutrition interactions: mucosal disruption, cytokines, and TLR signaling in a weaned murine model. *J. Parasitol.* **97**, 1113–1120 (2011).
6. Kirkpatrick, B. D. *et al.* Cryptosporidiosis stimulates an inflammatory intestinal response in malnourished Haitian children. *J. Infect. Dis.* **186**, 94–101 (2002).
7. Mondal, D., Haque, R., Sack, R. B., Kirkpatrick, B. D. & Petri, W. A. Attribution of malnutrition to cause-specific diarrheal illness: evidence from a prospective study of preschool children in Mirpur, Dhaka, Bangladesh. *Am. J. Trop. Med. Hyg.* **80**, 824–826 (2009).
8. Tzipori, S. & Ward, H. Cryptosporidiosis: biology, pathogenesis and disease. *Microbes Infect.* **4**, 1047–1058 (2002).
9. Watson, A. J. M., Duckworth, C. A., Guan, Y. & Montrose, M. H. Mechanisms of epithelial cell shedding in the Mammalian intestine and maintenance of barrier function. *Ann. N. Y. Acad. Sci.* **1165**, 135–142 (2009).
10. Delgado, M. E., Grabinger, T. & Brunner, T. Cell death at the intestinal epithelial front line. *FEBS J.* **283**, 2701–2719 (2016).
11. Chen, X.-M., Keithly, J. S., Paya, C. V. & LaRusso, N. F. Cryptosporidiosis. *N. Engl. J. Med.* **346**, 1723–1731 (2002).
12. Pardy, R. D., Wallbank, B. A., Striepen, B. & Hunter, C. A. Immunity to Cryptosporidium: insights into principles of enteric responses to infection. *Nat. Rev. Immunol.* **24**, 142–155 (2024).
13. Wahlström, A., Sayin, S. I., Marschall, H.-U. & Bäckhed, F. Intestinal Crosstalk between Bile Acids and Microbiota and Its Impact on Host Metabolism. *Cell Metab.* **24**, 41–50 (2016).
14. Chiang, J. Y. L. Bile acids: regulation of synthesis. *J. Lipid Res.* **50**, 1955–1966 (2009).
15. Makishima, M. *et al.* Identification of a nuclear receptor for bile acids. *Science* **284**, 1362–1365 (1999).
16. Parks, D. J. *et al.* Bile acids: natural ligands for an orphan nuclear receptor. *Science* **284**, 1365–1368 (1999).
17. Forman, B. M. *et al.* Identification of a nuclear receptor that is activated by farnesol metabolites. *Cell* **81**, 687–693 (1995).
18. Matsubara, T., Li, F. & Gonzalez, F. J. FXR signaling in the enterohepatic system. *Mol. Cell. Endocrinol.* **368**, 17–29 (2013).

19. Deng, S. *et al.* Cryptosporidium uses CSpV1 to activate host type I interferon and attenuate antiparasitic defenses. *Nat. Commun.* **14**, 1456 (2023).

20. Luo, J., Yang, H. & Song, B.-L. Mechanisms and regulation of cholesterol homeostasis. *Nat. Rev. Mol. Cell Biol.* **21**, 225–245 (2020).

21. Wang, B. & Tontonoz, P. Liver X receptors in lipid signalling and membrane homeostasis. *Nat. Rev. Endocrinol.* **14**, 452–463 (2018).

22. Tso, P. & Balint, J. A. Formation and transport of chylomicrons by enterocytes to the lymphatics. *Am. J. Physiol.* **250**, G715-726 (1986).

23. Ko, C.-W., Qu, J., Black, D. D. & Tso, P. Regulation of intestinal lipid metabolism: current concepts and relevance to disease. *Nat. Rev. Gastroenterol. Hepatol.* **17**, 169–183 (2020).

24. Li, H., Yu, X.-H., Ou, X., Ouyang, X.-P. & Tang, C.-K. Hepatic cholesterol transport and its role in non-alcoholic fatty liver disease and atherosclerosis. *Prog. Lipid Res.* **83**, 101109 (2021).

25. Jensen, R. G. Lipids in human milk. *Lipids* **34**, 1243–1271 (1999).

26. Liu, Z., Rochfort, S. & Cocks, B. Milk lipidomics: What we know and what we don't. *Prog. Lipid Res.* **71**, 70–85 (2018).

27. Chen, F. *et al.* Liver receptor homologue-1 mediates species- and cell line-specific bile acid-dependent negative feedback regulation of the apical sodium-dependent bile acid transporter. *J. Biol. Chem.* **278**, 19909–19916 (2003).

28. Spector, A. A. & Kim, H.-Y. Discovery of essential fatty acids. *J. Lipid Res.* **56**, 11–21 (2015).

29. Chen, X. M. & LaRusso, N. F. Mechanisms of attachment and internalization of Cryptosporidium parvum to biliary and intestinal epithelial cells. *Gastroenterology* **118**, 368–379 (2000).

30. Feng, H., Nie, W., Sheoran, A., Zhang, Q. & Tzipori, S. Bile acids enhance invasiveness of Cryptosporidium spp. into cultured cells. *Infect. Immun.* **74**, 3342–3346 (2006).

31. Ming, Z., Zhou, R. & Chen, X.-M. Regulation of host epithelial responses to Cryptosporidium infection by microRNAs. *Parasite Immunol.* **39**, (2017).

32. Thomson, S. *et al.* Bovine cryptosporidiosis: impact, host-parasite interaction and control strategies. *Vet. Res.* **48**, 42 (2017).

33. Annaba, F. *et al.* Modulation of ileal bile acid transporter (ASBT) activity by depletion of plasma membrane cholesterol: association with lipid rafts. *Am. J. Physiol. Gastrointest. Liver Physiol.* **294**, G489-497 (2008).

34. Cohen, D. E. Balancing cholesterol synthesis and absorption in the gastrointestinal tract. *J. Clin. Lipidol.* **2**, S1-3 (2008).

35. Hu, X. *et al.* A gut-derived hormone regulates cholesterol metabolism. *Cell* **187**, 1685-1700.e18 (2024).

36. Funkhouser-Jones, L. J. *et al.* Microbiota-produced indole metabolites disrupt mitochondrial function and inhibit Cryptosporidium parvum growth. *Cell Rep.* **42**, 112680 (2023).

37. Kalantari, N. *et al.* Association between Cryptosporidium infection and cancer: A systematic review and meta-analysis. *Parasitol. Int.* **74**, 101979 (2020).

38. van Best, N. *et al.* Bile acids drive the newborn's gut microbiota maturation. *Nat. Commun.* **11**, 3692 (2020).

39. Fontaine, F., Turjeman, S., Callens, K. & Koren, O. The intersection of undernutrition, microbiome, and child development in the first years of life. *Nat. Commun.* **14**, 3554 (2023).

40. VanDussen, K. L. *et al.* Neonatal Mouse Gut Metabolites Influence Cryptosporidium parvum Infection in Intestinal Epithelial Cells. *mBio* **11**, e02582-20 (2020).

41. Charania, R., Wade, B. E., McNair, N. N. & Mead, J. R. Changes in the Microbiome of Cryptosporidium-Infected Mice Correlate to Differences in Susceptibility and Infection Levels. *Microorganisms* **8**, 879 (2020).

42. Carey, M. A. *et al.* Megasphaera in the Stool Microbiota Is Negatively Associated With Diarrheal Cryptosporidiosis. *Clin. Infect. Dis. Off. Publ. Infect. Dis. Soc. Am.* **73**, e1242–e1251 (2021).

43. Wang, Y. *et al.* Delivery of parasite Cdg7_Flc_0990 RNA transcript into intestinal epithelial cells during Cryptosporidium parvum infection suppresses host cell gene transcription through epigenetic mechanisms. *Cell. Microbiol.* **19**, (2017).

44. Ferguson, S. H. *et al.* Interferon-λ3 Promotes Epithelial Defense and Barrier Function Against Cryptosporidium parvum Infection. *Cell. Mol. Gastroenterol. Hepatol.* **8**, 1–20 (2019).

45. Zhu, G. *et al.* Expression and functional characterization of a giant Type I fatty acid synthase (CpFAS1) gene from Cryptosporidium parvum. *Mol. Biochem. Parasitol.* **134**, 127–135 (2004).

46. Chen, X.-M. *et al.* Cryptosporidium parvum invasion of biliary epithelia requires host cell tyrosine phosphorylation of cortactin via c-Src. *Gastroenterology* **125**, 216–228 (2003).

47. Lacroix, S., Mancassola, R., Naciri, M. & Laurent, F. Cryptosporidium parvum-specific mucosal immune response in C57BL/6 neonatal and gamma interferon-deficient mice: role of tumor necrosis factor alpha in protection. *Infect. Immun.* **69**, 1635–1642 (2001).

48. Kapel, N. *et al.* Kinetics of mucosal ileal gamma-interferon response during cryptosporidiosis in immunocompetent neonatal mice. *Parasitol. Res.* **82**, 664–667 (1996).

49. Yu, G., Wang, L.-G., Han, Y. & He, Q.-Y. clusterProfiler: an R package for comparing biological themes among gene clusters. *Omics J. Integr. Biol.* **16**, 284–287 (2012).

50. Liberzon, A. *et al.* The Molecular Signatures Database (MSigDB) hallmark gene set collection. *Cell Syst.* **1**, 417–425 (2015).

51. Hänzelmann, S., Castelo, R. & Guinney, J. GSVA: gene set variation analysis for microarray and RNA-seq data. *BMC Bioinformatics* **14**, 7 (2013).

52. Wang, J. *et al.* Identification and evaluation of a lipid-lowering small compound in preclinical models and in a Phase I trial. *Cell Metab.* **34**, 667-680.e6 (2022).

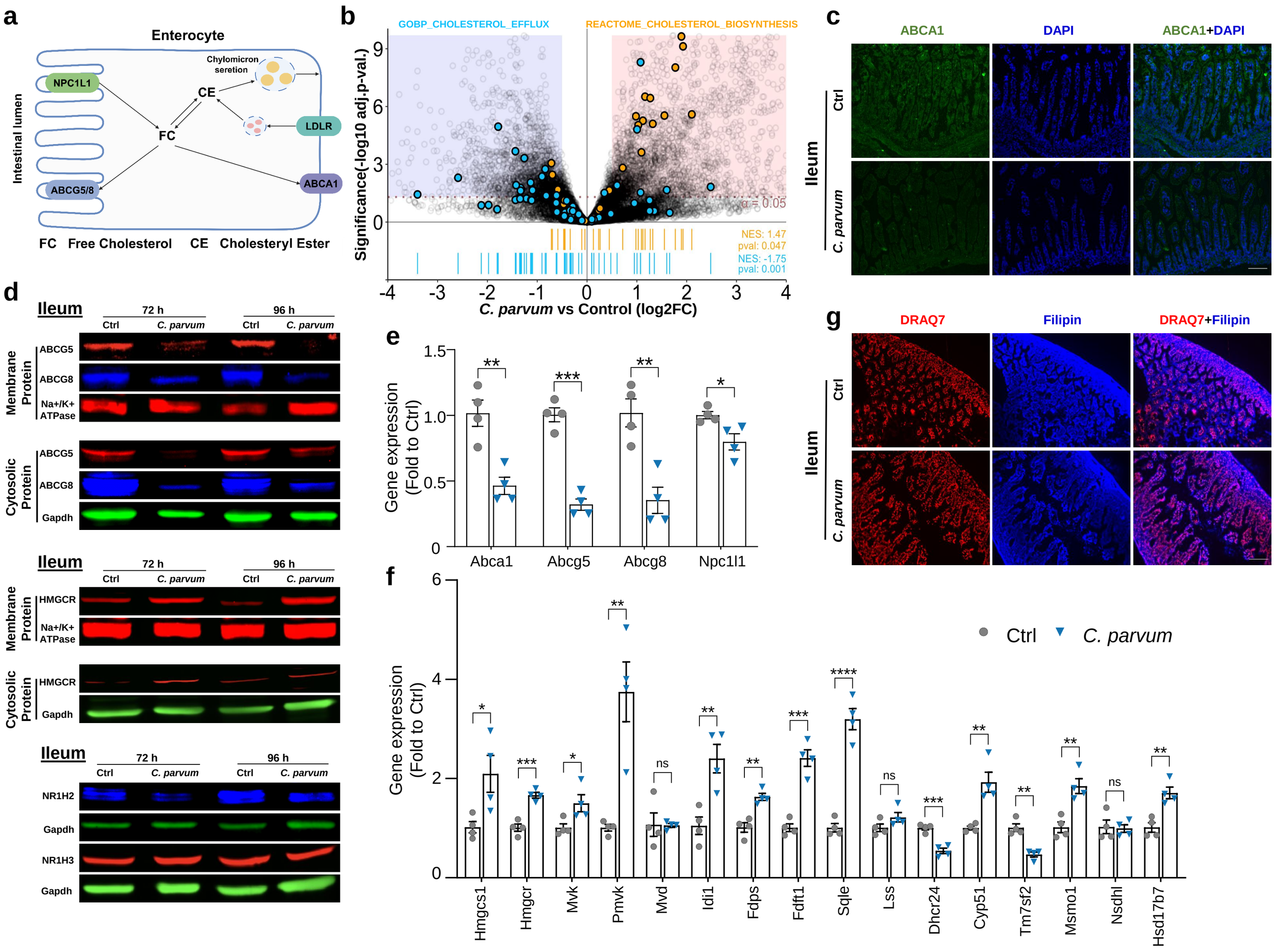

Fig. 1 | *C. parvum* infection disrupts cholesterol homeostasis in ileum

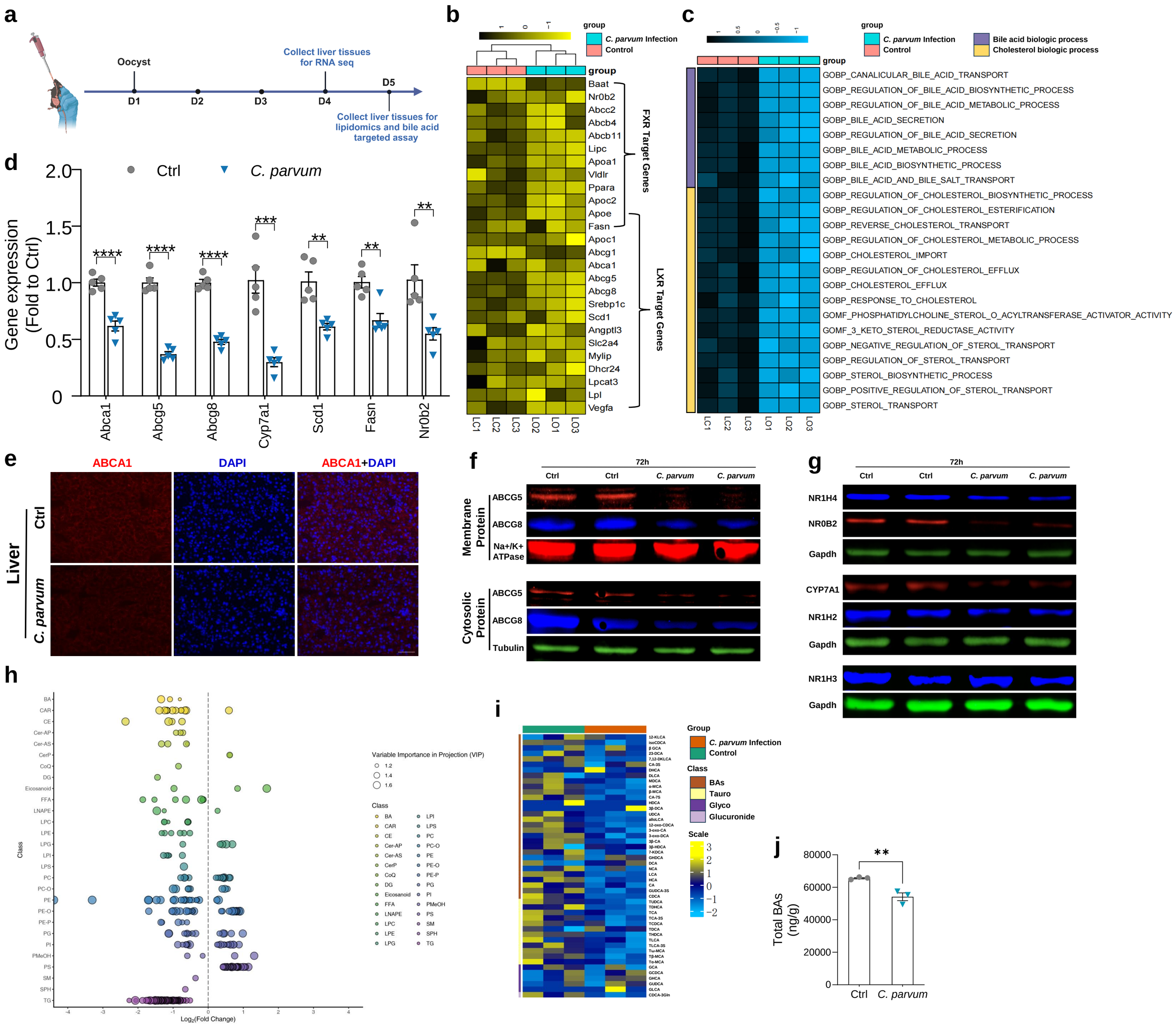

Fig. 2 | *C. parvum* intestinal infection causes dysregulation of cholesterol and bile acid homeostasis in the liver

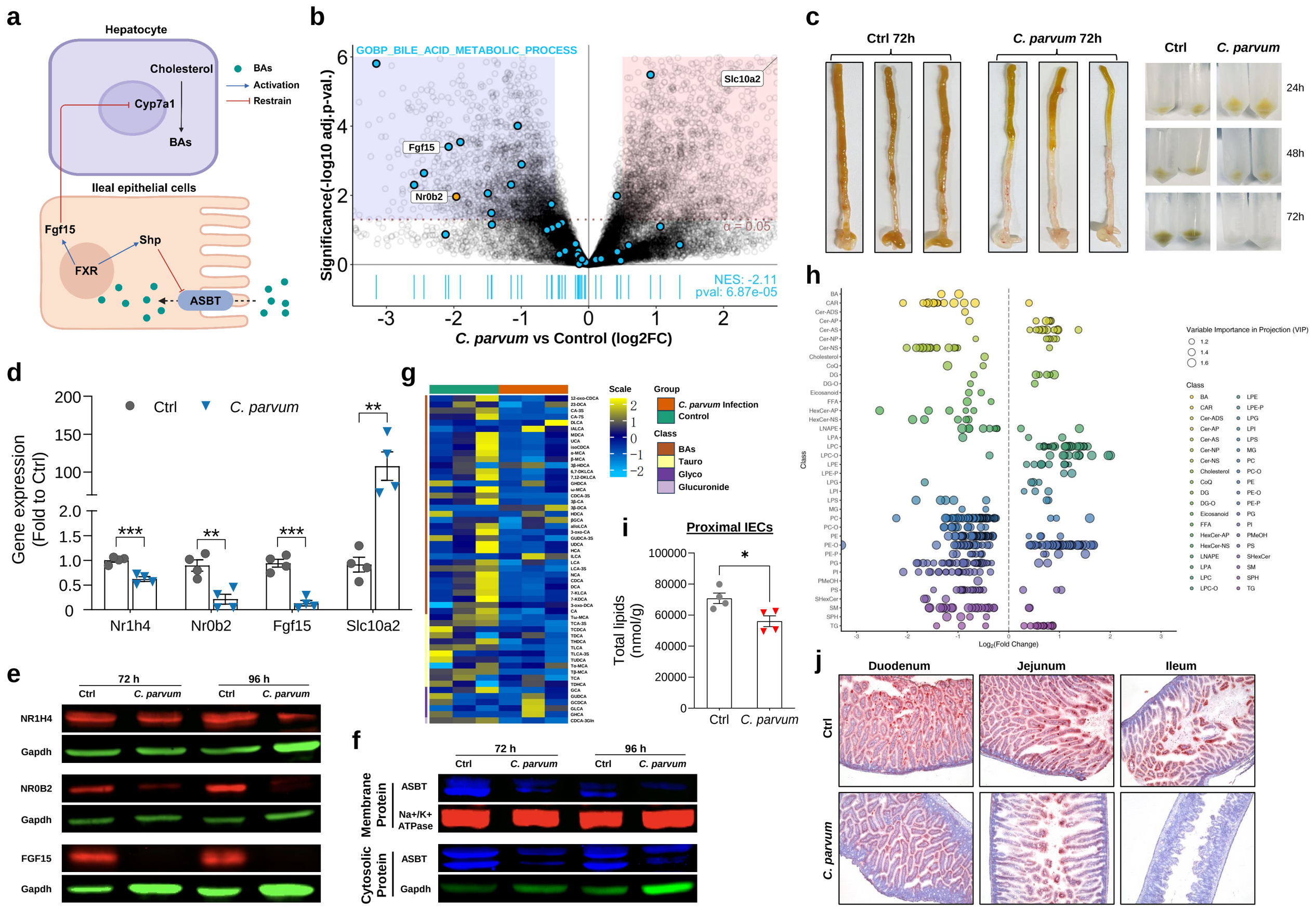

Fig. 3 | *C. parvum* infection decreases BA levels in the small intestine and reduces the absorption of dietary lipids

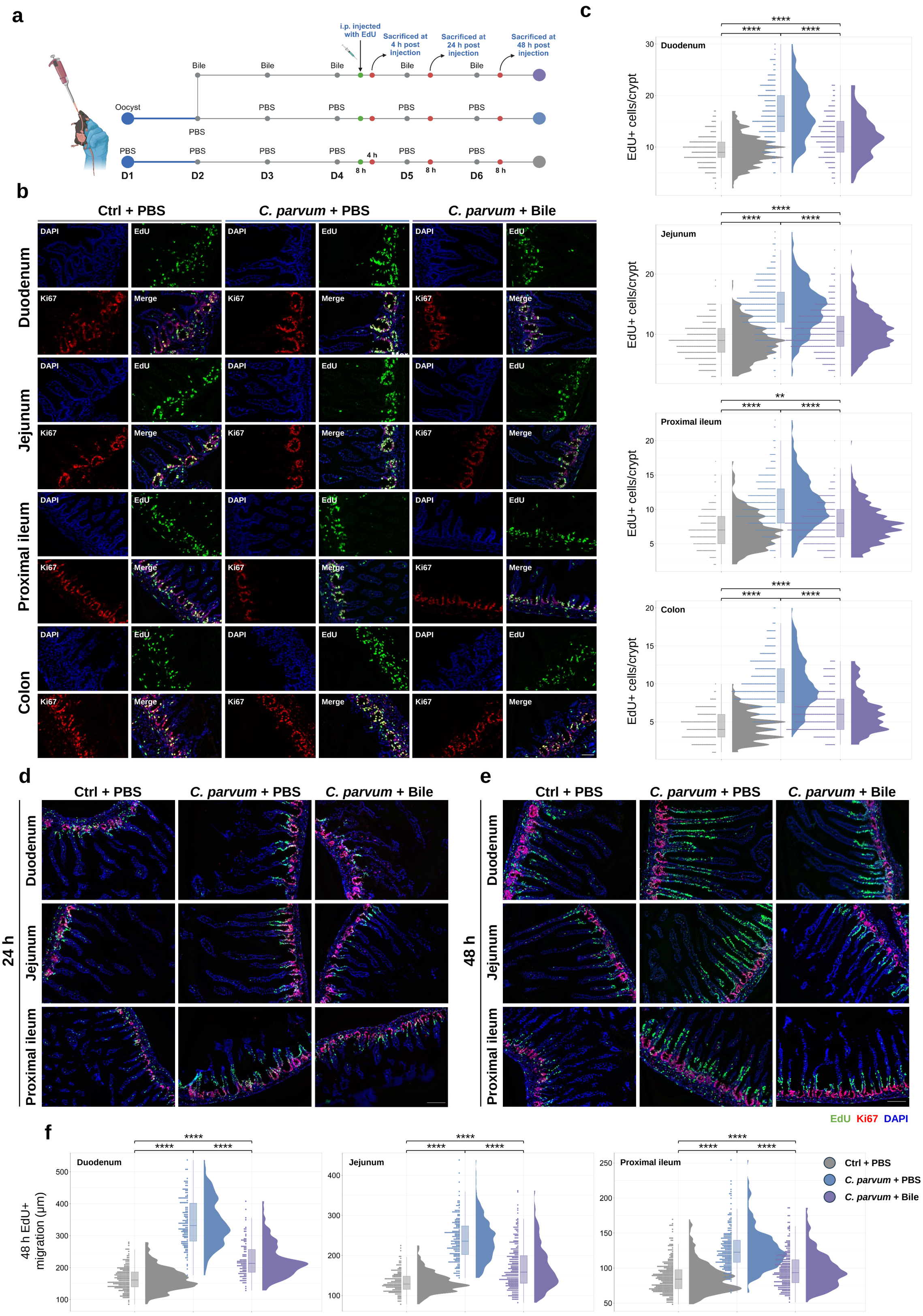

Fig. 4 | Bile intervention attenuates the dysregulated homeostasis in the intestinal epithelium following *C. parvum* infection

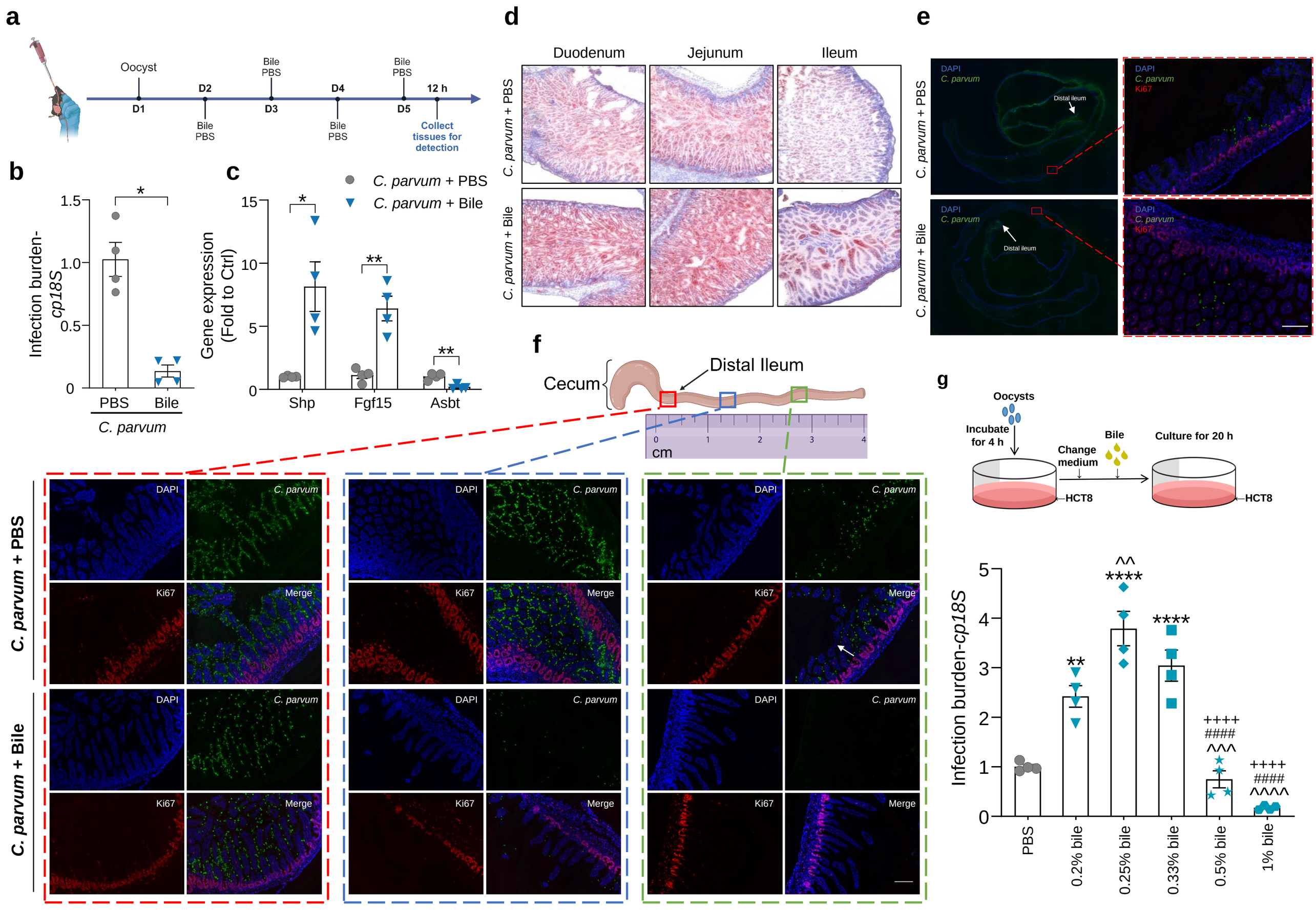

Fig. 5 | Bile intervention promotes intestinal anti-*C. parvum* defense and prevents decreased lipid absorption following infection

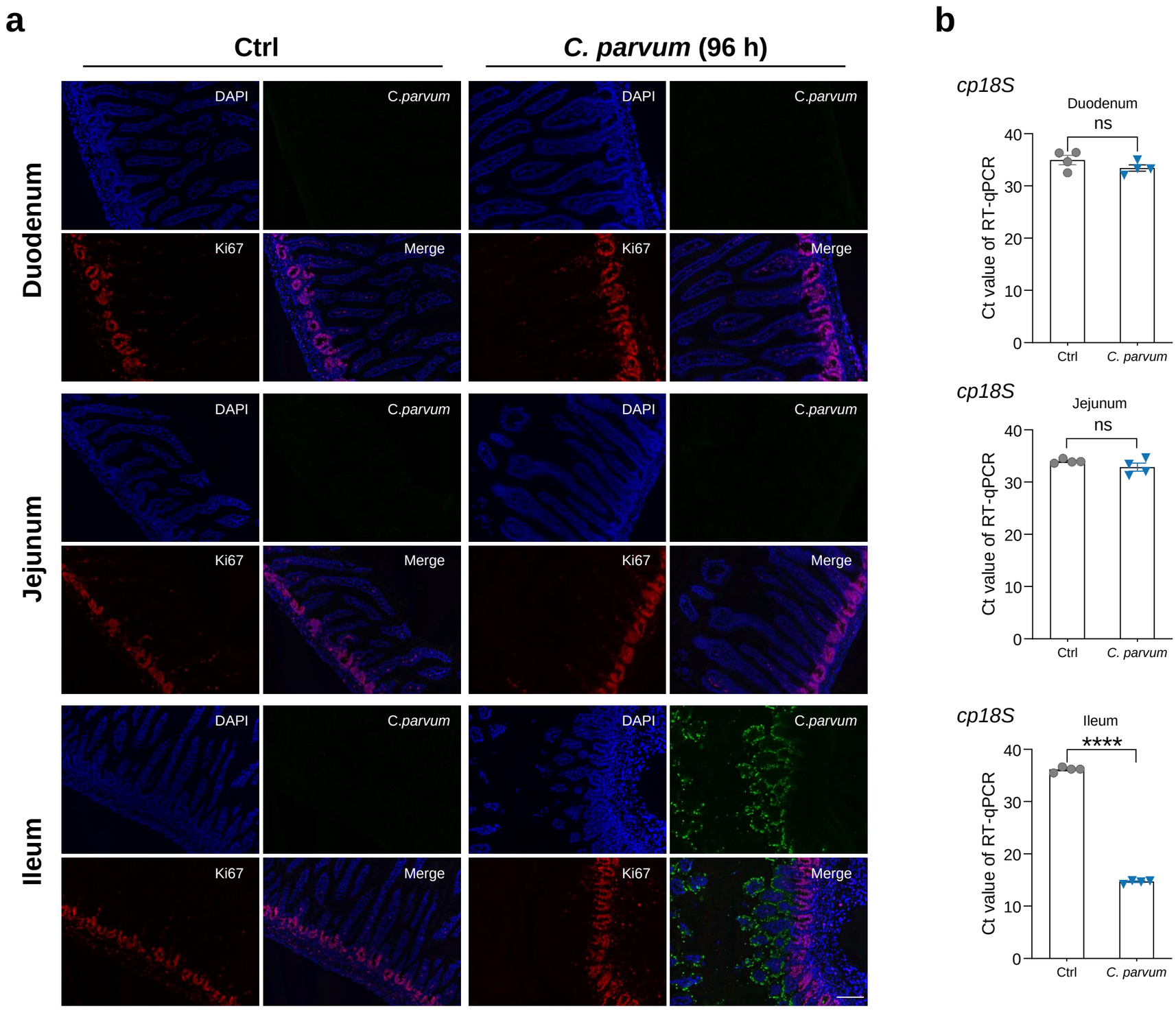

Extended Data Fig. 1 | *C. parvum* intestinal infection burden in neonates with and without *C. parvum* infection

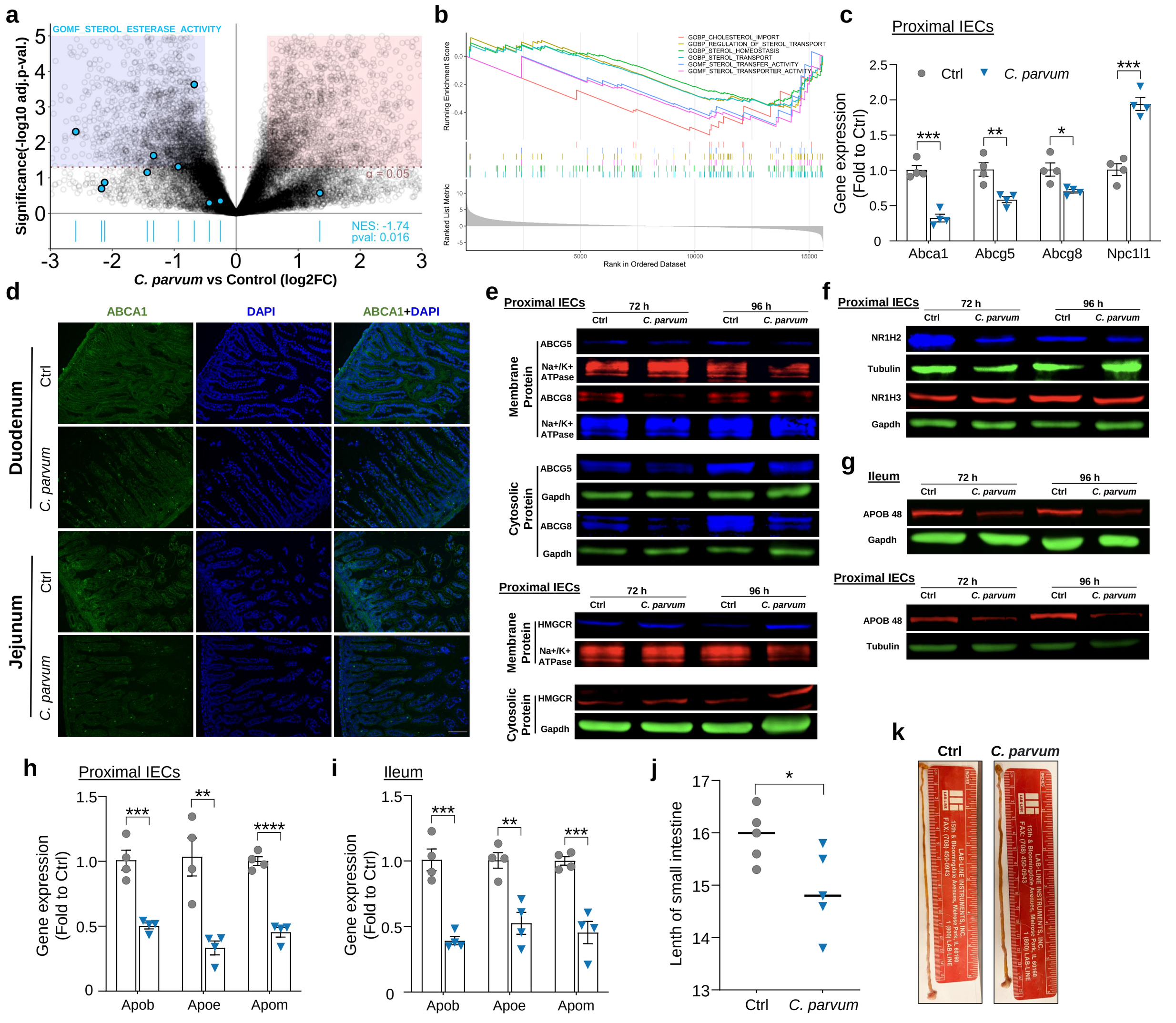

Extended Data Fig. 2 | *C. parvum* infection disrupts cholesterol homeostasis in the small intestine

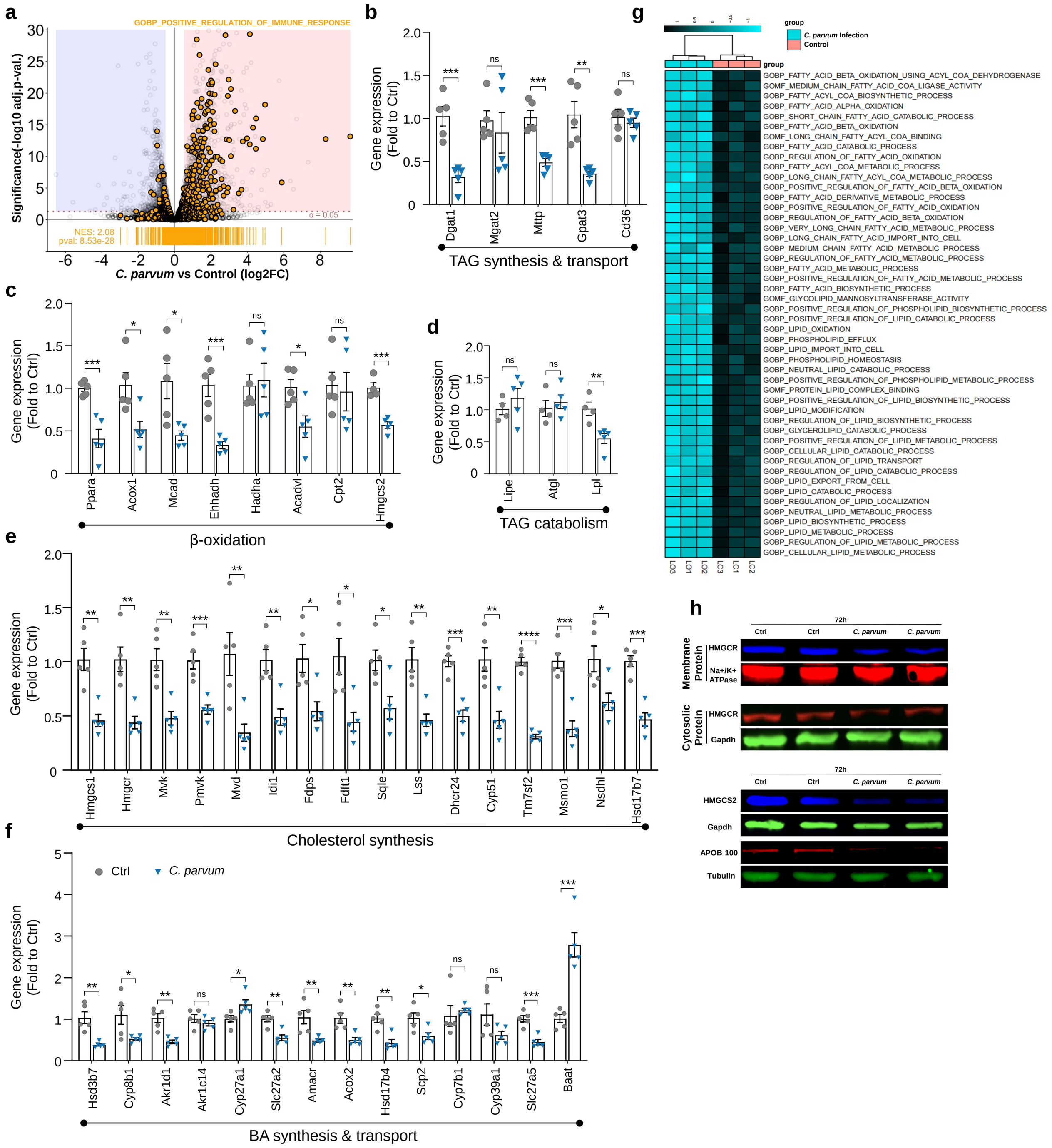

Extended Data Fig. 3 | *C. parvum* infection alters hepatic genes expression

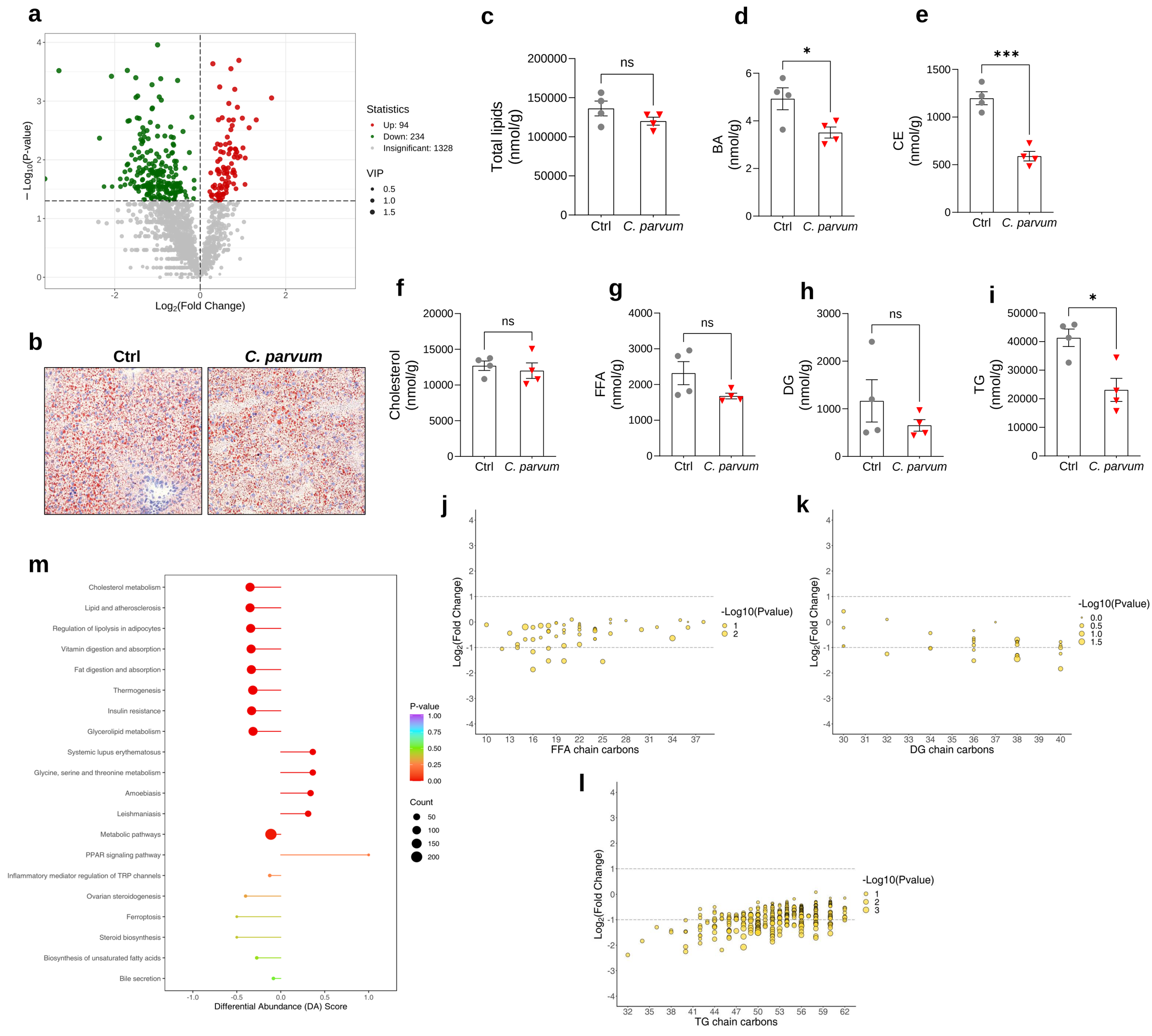

Extended Data Fig. 4 | Impaired lipid homeostasis in the livers of *C. parvum* infected mice

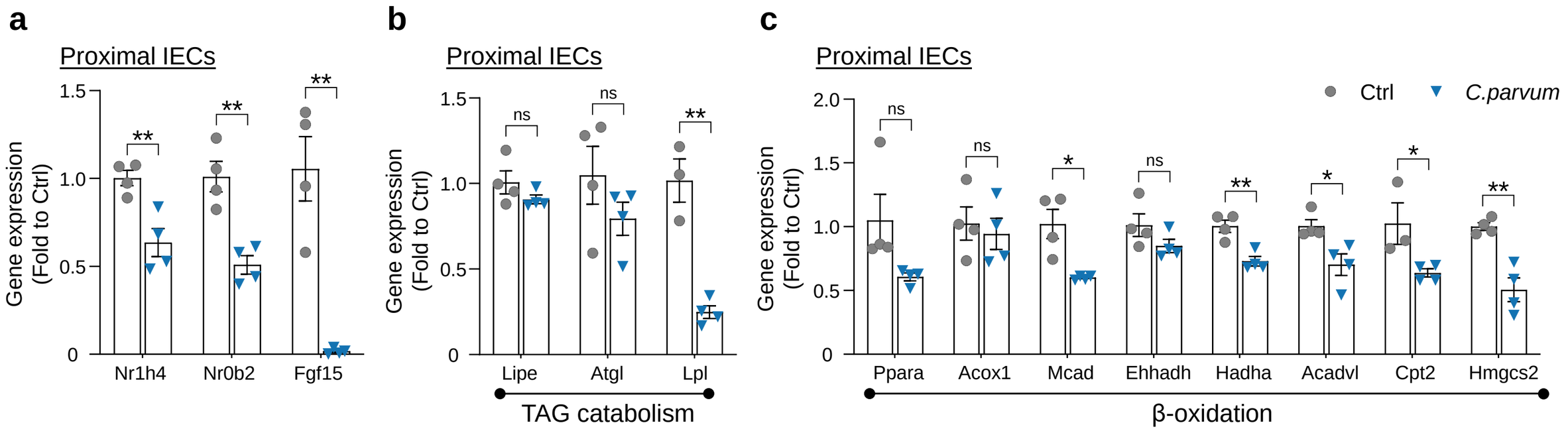

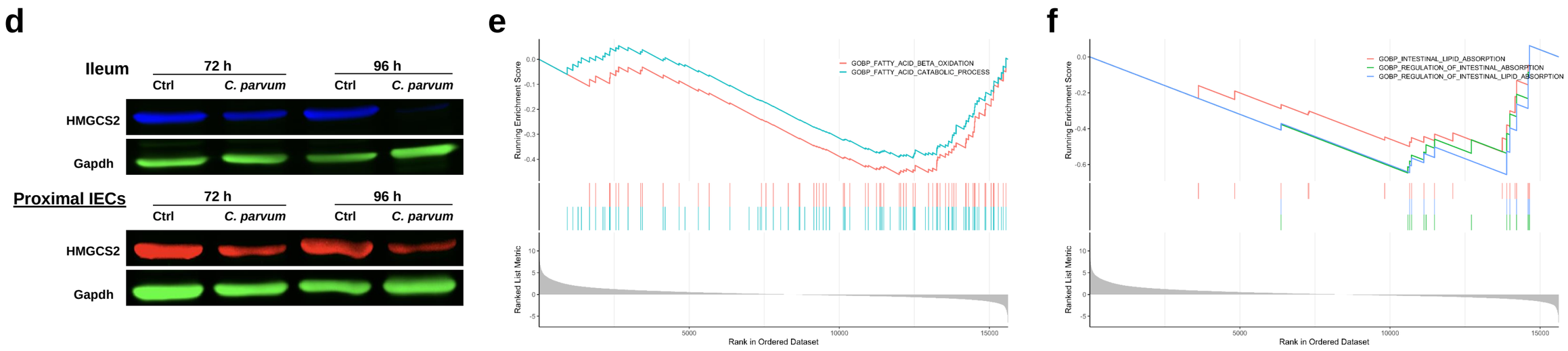

Extended Data Fig. 5 | *C. parvum* infection alters intestinal lipid metabolic genes expression

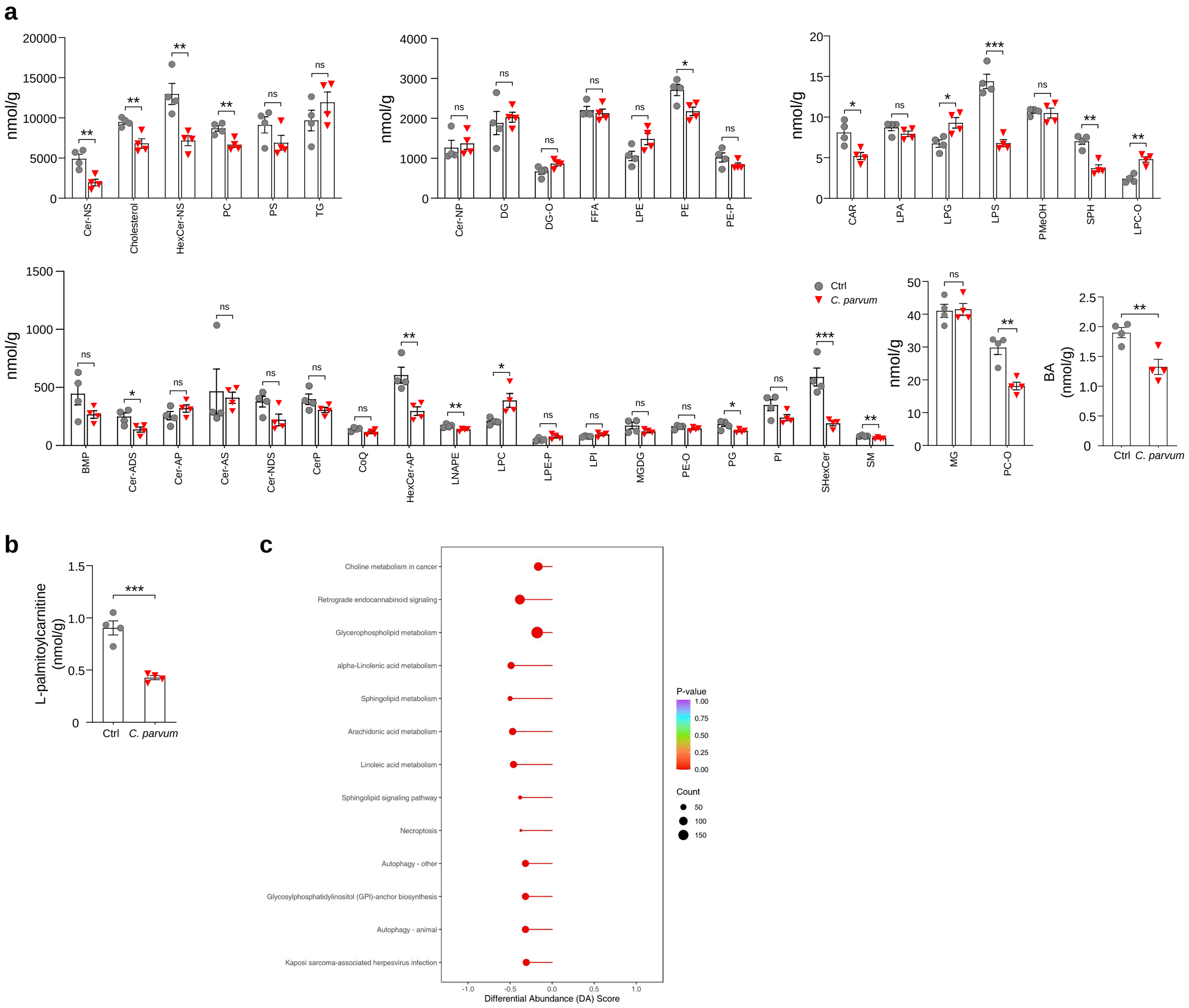

Extended Data Fig. 6 | Impaired lipid homeostasis in the proximal IECs of *C. parvum* infected mice

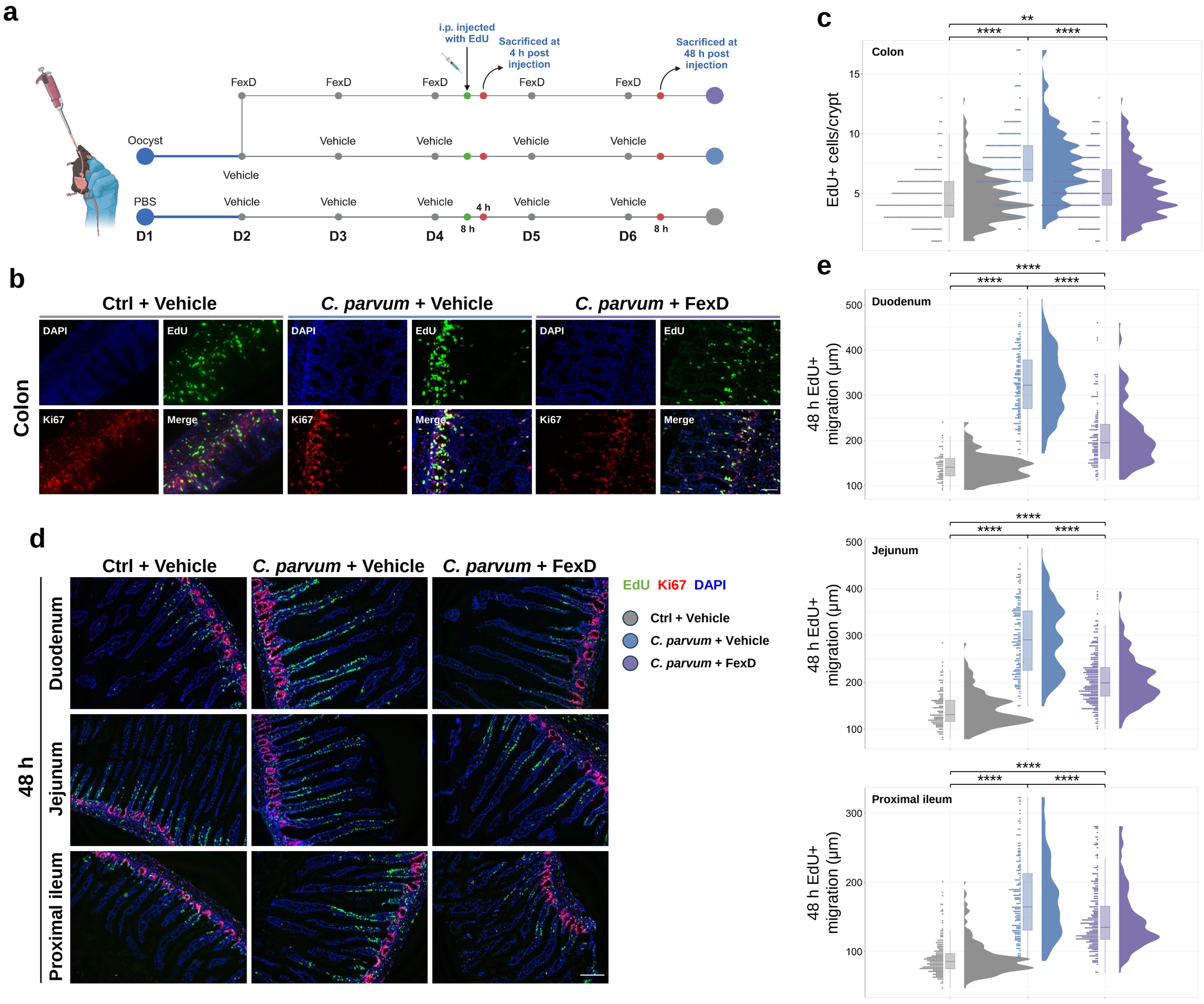

Extended Data Fig. 7 | FXR activation attentuates the dysregulated homeostasis in the intestinal epithelium following *C. parvum* infection

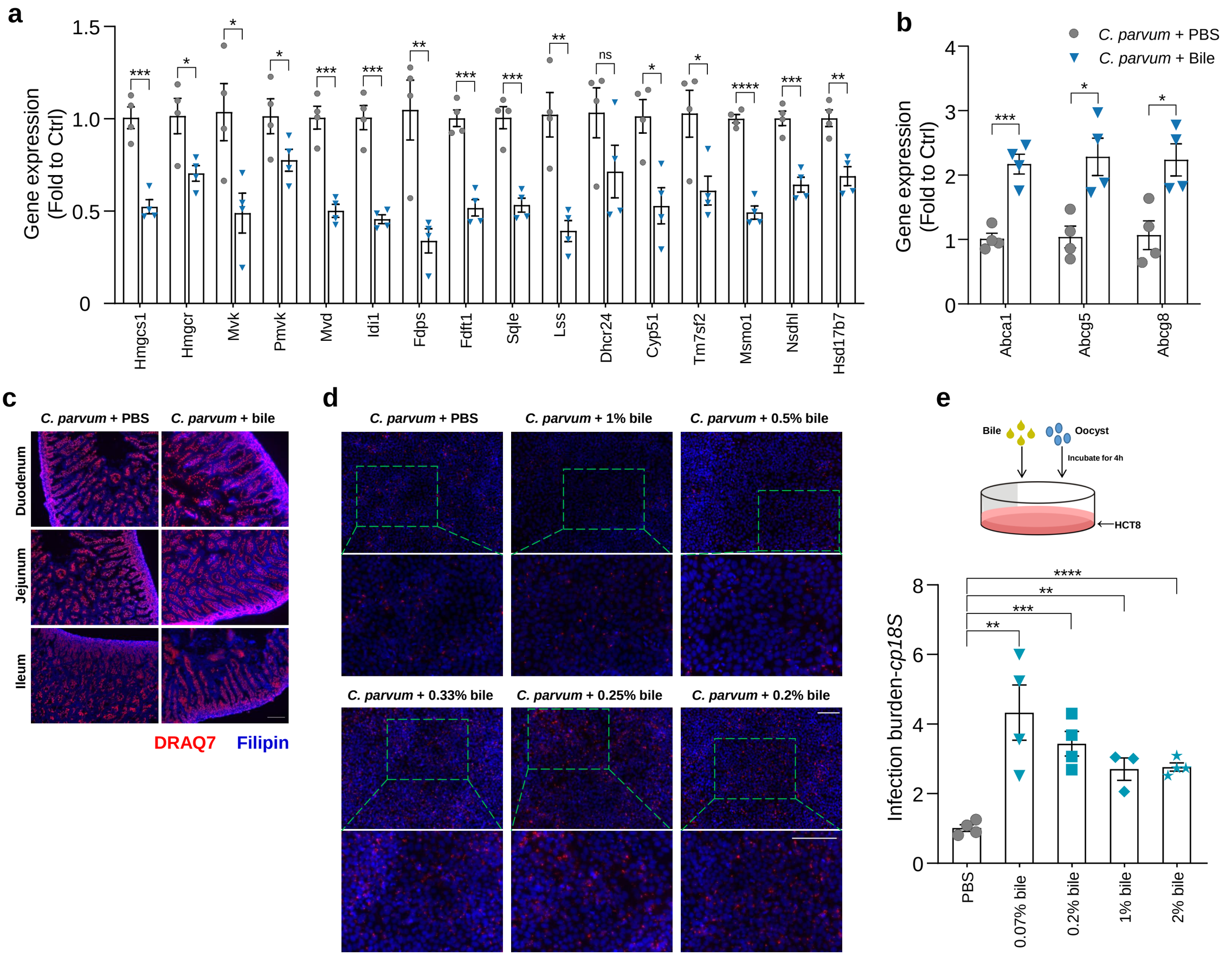

Extended Data Fig. 8 | Effects of bile on *C. parvum* infection

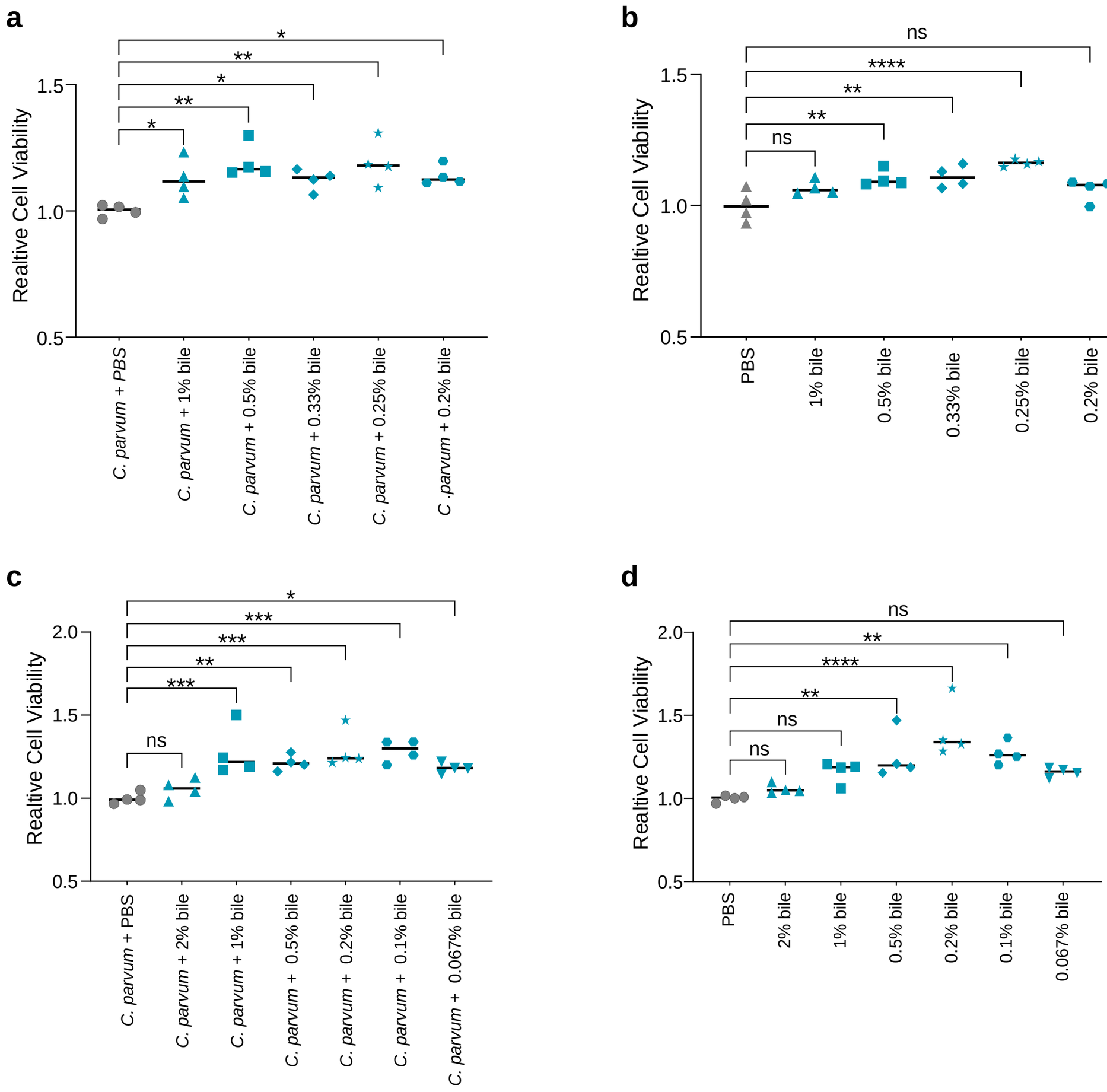

Extended Data Fig. 9 | Effects of bile on HCT-8 cells viability with or without *C. parvum* infection